



# P-T-time evolution of the Mejillones Metamorphic Complex: Insights into Late Triassic to Early Jurassic orogenic processes in northern Chile



M. Calderón<sup>a,\*</sup>, H.-J. Massonne<sup>b</sup>, F. Hervé<sup>a,c</sup>, T. Theye<sup>b</sup>

<sup>a</sup> Carrera de Geología, Facultad de Ingeniería, Universidad Andres Bello, Sazie 2119, Santiago, Chile

<sup>b</sup> Institut für Mineralogie und Kristallchemie, Universität Stuttgart, Azenbergstrasse 18, D-70174 Stuttgart, Germany

<sup>c</sup> Departamento de Geología, Universidad de Chile, Casilla 13518, Correo 21, Santiago, Chile

## ARTICLE INFO

### Keywords:

Morro Jorgiño tectonic unit  
Barrovian-type metamorphism  
P-T pseudosections  
Th-U-Pb monazite geochronology

## ABSTRACT

Better constrained pressure-temperature (P-T) histories of metamorphic complexes along the Andean continental margin are important for understanding the late Paleozoic and Mesozoic tectonic evolution of the southwestern margin of Gondwana. The Mejillones Metamorphic Complex of the northern Chilean Coastal Cordillera is composed of two tectonic units, the Morro Mejillones and Morro Jorgiño blocks. These units are bound by the NW-trending Caleta Herradura fault and show distinctly metamorphic ages and thermal evolution. The Morro Mejillones block was metamorphosed at low pressure conditions (andalusite-sillimanite series) during the intrusion of tonalitic plutons at ca. 208 Ma, as indicated by available geochronological data. In contrast, the Morro Jorgiño block comprises amphibolite-facies schists, gneisses and foliated metabasites with characteristic garnet-bearing mineral assemblages. For garnet-bearing pelitic gneisses, a clockwise P-T path has been determined from pseudosection modelling in the MnNCKFMASHTO system. The proposed evolution is characterized by a pressure increase from 7.5 to 8.5 kbar at increasing temperatures from 585 to 615 °C. Decompression to 6 kbar followed, accompanied by heating to 630–640 °C. Electron microprobe Th-U-Pb in-situ dating of high-Y monazite grains yielded a weighted average age of ca. 190 ± 4 Ma, which is interpreted as the age of tectonic burial of metamorphic rocks of the Morro Jorgiño tectonic unit. We infer that the block was buried to ~25 km depth through contractional deformation of the continental edge in a subduction zone, likely linked to the docking of the Mejillonia terrane. Rapid exhumation followed and the ensuing juxtaposition of both tectonic units was controlled by Jurassic transtensional activity of the Atacama Fault System.

## 1. Introduction

The late Paleozoic to early Mesozoic geological evolution of northern Chile is closely related to transient tectonic processes that acted along the western Gondwana margin between the final stage of the assembly of Pangea (ca. 320–280 Ma) and the onset of the supercontinent break-up (Li and Powell, 2001; Murphy et al., 2009). Petrotectonic associations in the Argentine and Chilean Andes record an early to middle Permian subduction-related orogenic phase (San Rafael phase of Llambías and Sato, 1995; Gregori and Benedini, 2013) followed by a regional middle Permian to Triassic extensional orogenic collapse. The generalized extensional phase continued until the Late Triassic, resulting in the development of widely distributed NNW-SSE orientated extensional rift basins in Argentina and Chile (Charrier, 1979; Uliana and Biddle, 1988; Mpodozis and Ramos, 1989; Suárez and Bell, 1992). This major phase of lithospheric extension along the convergent margin of South America was coeval with a period of relatively slow plate convergence rates (Charrier et al., 2007).

The aforementioned late Paleozoic to Triassic tectonic evolution was accompanied by episodes of supra-subduction zone magmatism that occurred during discrete time interval – mostly recognized in the high Andes – during Carboniferous, Permian, Lower Triassic and Upper Triassic time (Munizaga et al., 2008; Tomlinson and Blanco, 2008; Hervé et al., 2014; Maksaev et al., 2014; Del Rey et al., 2016; Pankhurst et al., 2016). An apparent trench-ward migration of magmatism culminated with emplacement of Upper Triassic–Lower Jurassic bimodal igneous suites as exposed along the Coastal Cordillera (Vergara et al., 1991; Gana, 1991; Villegas and Parada, 1993; Godoy and Lara, 1998; Vásquez et al., 2011; Casquet et al., 2014; Escribano et al., 2013; Firth et al., 2015). The original architecture of the late Paleozoic fore-arc system was modified by Mesozoic extensional and contractional events (Willner et al., 2011) and batholith construction.

Between latitudes 21°S and 24°S, the Proterozoic metamorphic rocks at Sierra de Moreno (Fig. 1A) are intruded by early Ordovician granitoids correlated with the Famatinian magmatism that occurred in

\* Corresponding author.

E-mail address: mauricio.calderon@unab.cl (M. Calderón).

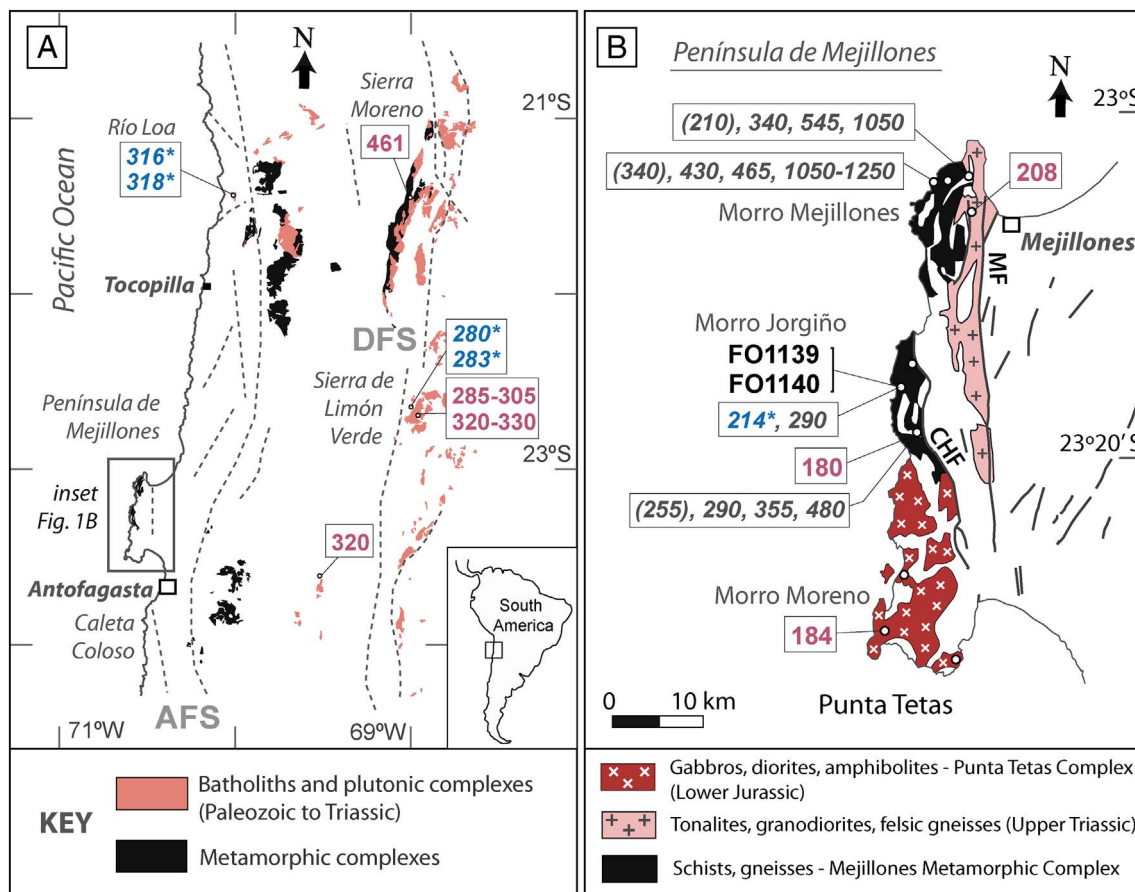


**Fig. 1.** (A) Geological sketch map of the igneous and metamorphic outcrops in northern Chile (modified from Sernageomin, 2003 and Pankhurst et al., 2016). The dotted lines represent the significant fault traces of the Atacama Fault System (AFS) and Domeyko Fault System (DFS). (B) Simplified geological map of the Mejillones Peninsula located north of the city of Antofagasta. Pre-Late Jurassic lithological units are shown. Heavy line-work represents various generations of brittle and ductile faults belonging to the Atacama Fault System. Abbreviations are: MF, Mejillones Fault; CHF, Caleta Herradura Fault. Numbers (in Ma, for those in boxes) refer to SHRIMP and LA-ICP-MS U-Pb zircon ages reported by Makaev et al. (2014), Morandé (2014), Casquet et al. (2014) and Pankhurst et al. (2016). Those in red are igneous crystallization ages. Asterisks point to metamorphic ages. Numbers in italic are the main groups of detrital zircon ages in metasedimentary rocks; those in parentheses (younger detrital zircon ages) may be insignificant. (For interpretation of the references to color in this figure legend, the reader is referred to the web version of this article.)

northern Argentina (Pankhurst et al., 2016). Subsequent Carboniferous and Permian magmatism was coeval with crustal deformation and high-grade metamorphism of pelitic and basaltic protoliths. These resulting metamorphic rocks crop out near the mouth of Río Loa and in the Sierra Limón Verde (Lucassen et al., 1999; Hervé et al., 2007; Lucassen et al., 2011; Soto, 2013; Morandé, 2014; Pankhurst et al., 2016). Triassic and Jurassic igneous and metamorphic events are also known in rocks from Península de Mejillones and Caleta Coloso (Lucassen and Franz, 1996; Casquet et al., 2014).

There are a number of outstanding questions with respect to the proposed geodynamic models for the Chilean convergent margin of Gondwana in Triassic times. For instance, such models have considered that subduction has not occurred continuously, but rather, subduction ceased prior to resumed subduction of the Phoenix Plate and onset of Andean-type arc magmatism in the Early Jurassic (Charrier et al., 2007). The implications of long-lived versus episodic subduction processes along a single convergent margin affect our understanding of paleogeography, crust-mantle interactions, supercontinent assembly, and cessation/initiation of subduction zones. Further studies of the metamorphic rocks and their P-T paths, coupled with precise geochronology, are essential to understanding the evolution of the aforementioned subduction setting and to detect changes in the configuration of tectonic conditions. New data presented here for the Mejillones Metamorphic Complex in northern Chile allow us to better constrain Late Triassic to Early Jurassic crustal processes along the continental edge of the convergent margin of South America. Based on electron

microprobe data, P-T pseudosection calculations, Th-U-Pb monazite dating and previous U-Pb zircon geochronological data (Casquet et al., 2014), we propose a model for the tectonic evolution of the Mejillones Metamorphic Complex that involves fore-arc crustal attenuation and subsequent crustal thickening close to the continental edge.

## 2. Geological context and the Mejillones Metamorphic Complex

During the latest Triassic, in northern Chile, silicic magmatism was coeval with transitional continental-marine sedimentation within the northwest-oriented El Profeta and Cifuncho rift basins (Suárez and Bell, 1992; Charrier et al., 2007; Escrivano et al., 2013). These basin successions contain fluvial and alluvial conglomeratic deposits along their western flanks, overlain by platform turbidites and limestones with basal intercalations of Upper Triassic tuffs (Cifuncho and Pan de Azúcar formations; Naranjo and Puig, 1984; Contreras et al., 2013). Along the eastern flanks of the basins, clastic continental rocks overlain by hemipelagic calcareous sedimentary successions were deposited in a platform environment (El Profeta Formation; Chong and von Hillebrandt, 1985; Marinovic et al., 1995). The rift basins evolved to intra-arc or back-arc basins during the Jurassic (Tarapacá basin; Vicente, 2006), coeval with the emplacement of voluminous successions of calc-alkaline basaltic andesites, andesites and thick coarse-volcaniclastic successions of the La Negra Formation (García, 1967; Naranjo and Puig, 1984; Marinovic et al., 1995; Oliveros et al., 2007; Parada et al., 2007). This interval of upper plate magmatism is thought

to have occurred under transtension related to the Atacama Fault System during southeast-directed oblique subduction of the Phoenix plate (Hervé, 1987; Brown et al., 1993; Scheuber et al., 1994; Lucassen and Franz, 1996; Scheuber and González, 1999).

The Mejillones Metamorphic Complex crops out in the Mejillones Peninsula of the northern Coastal Cordillera of Chile (Fig. 1B), and constitutes rugged topography with peaks up to nearly 1000 m above sea level. The complex is separated from the main coastline of the continental margin through the partly exhumed latest Cenozoic Mejillones fore-arc basin, which, since middle Miocene-Pliocene times, has been filled mainly with shallow-marine successions coeval with normal faulting along steeply dipping graben-like structures (Hartley and Jolley, 1995). The sedimentary successions were subsequently uplifted since ca. 2 Ma (Clift and Hartley, 2007) and marine terraces are preserved on the top of the northern part of the peninsula at ~300 m above sea level.

The Mejillones Metamorphic Complex comprises two isolated outcrop areas of basement rocks, each with contrasting metamorphic facies. The two areas are bound by the NW-trending Caleta Herradura Fault and the north-south-trending Mejillones Fault (cf. Damm et al., 1990; Hervé et al., 2007; Cortés et al., 2007) (Fig. 1B). The northern outcrop area at Morro Mejillones is composed mainly of low-grade metaturbidites, delimited to the east by a roughly north-south-trending belt of Late Triassic plutons (Cortés et al., 2007; Casquet et al., 2014). A contact metamorphic aureole is superimposed on the low-grade metaturbidites, with biotite, andalusite–sillimanite, and K-feldspar–sillimanite zones, and gneissic components restricted to the contact with Late Triassic granitoids (Baeza, 1984; Baeza and Pichowiak, 1988). The metamorphic rocks show two phases of foliation and folding.  $S_0$ – $S_1$  is a compositional banding represented by alternating thicker quartz-rich and thinner biotite-rich layers. Folds are isoclinal and east-vergent. Near the axial zone, a foliation ( $S_2$ ) overprints  $S_0$ – $S_1$ . Intersection lineations are common. These metamorphic rocks are intruded by the Morro Mejillones pluton, a N–S elongated coarse grained biotite-hornblende tonalite body dated at ca. 208 Ma (Casquet et al., 2014).

The southern outcrops at Morro Jorgiño (Fig. 1B) consist of tightly folded schists, gneisses, amphibolites, and quartzites, intruded by garnet-bearing leucogranite sheets (Fig. 2). Metamorphic rocks show a penetrative  $S_1$  compositional banding represented by alternating thicker quartz-plagioclase-rich and thinner garnet-bearing biotite-rich bands. Similar structures are preserved in cordierite-bearing schists and gneisses, some with retrogressed porphyroblasts of garnet and retrograde white mica and chlorite. Folds are isoclinal and, near the axial zone, show an overprinting foliation  $S_2$ . Metabasites are fine-grained with a penetrative foliation. Leucogranites are concordant or slightly discordant to the external foliation and have been dated at ca. 180 Ma (Casquet et al., 2014). A regional Barrovian-type metamorphic zoning including biotite, garnet and kyanite zones has been described by Baeza

and Pichowiak (1988), who estimated metamorphic peak P–T conditions of 4–6 kbar and 400–600 °C. Based on petrogenetic grids for amphibolites by Winkler (1976) and the stability field of relevant phases, Damm et al. (1990) estimated that these P–T conditions exceeded 6 kbar and reached 600–700 °C. The bulk-rock geochemical composition of the amphibolites has been interpreted to indicate that their protoliths were tholeiitic basalts formed in a supra-subduction zone setting (Damm et al., 1990).

The metamorphic rocks are delimited to the south by Lower Jurassic (ca. 184 Ma) dioritic to gabbroic plutons of the Punta Tetas complex (Cortés et al., 2007; Casquet et al., 2014) (Fig. 1B). These plutons crop out at Morro Moreno and display magmatic and high temperature metamorphic foliations. Similar rocks and structural features have been recognized in the Bolfin metamorphic complex, at Caleta Coloso (Fig. 1A), interpreted as the product of early Jurassic magmatic arc metamorphism (Lucassen and Franz, 1996).

### 3. Methods

Chemical compositions of minerals were obtained on selected rock samples from Morro Jorgiño using a CAMECA SX100 electron microprobe with 5 wavelength-dispersive spectrometers at Universität Stuttgart, Germany. Operating conditions were an accelerating voltage of 15 kV, a beam current of 15 nA, a beam size of 7–10  $\mu\text{m}$  or a focussed beam (for very small crystals), and 20 s counting time on the peak and on the background of each element. The respective standards used to calibrate these analyses were wollastonite (Si, Ca), orthoclase (K), albite (Na), rhodonite (Mn), synthetic  $\text{Cr}_2\text{O}_3$  (Cr), synthetic  $\text{TiO}_2$  (Ti), hematite (Fe), baryte (Ba), synthetic  $\text{MgO}$  (Mg), synthetic  $\text{Al}_2\text{O}_3$  (Al) and synthetic  $\text{NiO}$  (Ni). The PaP correction procedure provided by Cameca was applied. Analytical errors of the applied method were reported by Massonne (2012). Representative data are reported in Tables 1 and 2; the chemical bulk compositions of rock samples, required for the calculation of P–T pseudosections, were determined with a PHILIPS PW 2400 X-ray fluorescence (XRF) spectrometer at Universität Stuttgart using glass discs prepared from rock powder and Spectromelt®. Results on major oxide compositions are presented in Table 3.

Electron microprobe Th–U–Pb in-situ dating of monazite crystals in biotite–garnet gneisses, considering a total of 36 spot analyses, was carried out using the aforementioned Cameca SX100 electron microprobe. An accelerating voltage of 20 kV, a beam current of 200 nA, and a spot size of 10  $\mu\text{m}$  were chosen as operating conditions. We determined concentrations of S (K $\alpha$ ), Th (M $\alpha$ ), P (K $\alpha$ ), U (M $\beta$ ), Ca (K $\alpha$ ), Pb (M $\alpha$ ), Y (L $\alpha$ ), Si (K $\alpha$ ), La (L $\alpha$ ), Ce (L $\alpha$ ), Nd (L $\beta$ ), Sm (L $\beta$ ), Gd (L $\beta$ ), Dy (L $\beta$ ), and Pr (L $\beta$ ) applying natural and synthetic standards such as phosphates for the determination of lanthanides (see, e.g. Massonne et al., 2007a). The obtained apparent ages, with their  $1\sigma$  errors (solely based on counting statistics), were used to define a relative probability age curve and

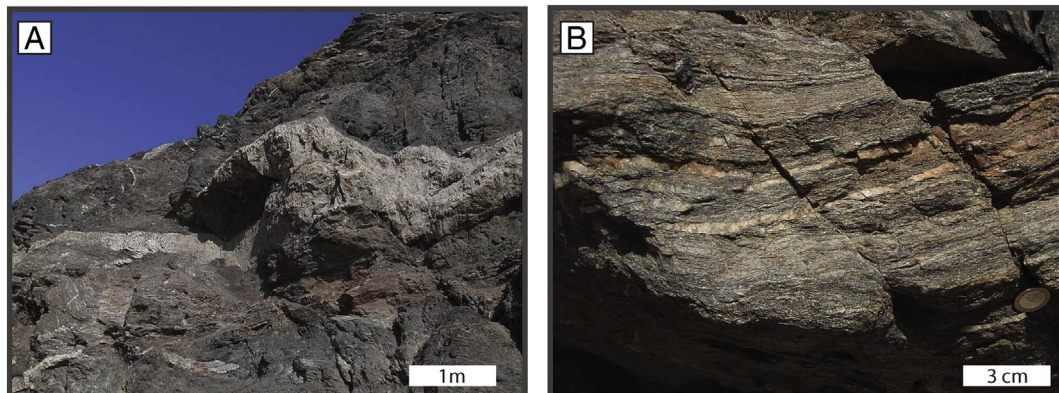


**Fig. 2.** Field photographs of different rocks of the Mejillones Metamorphic Complex at Morro Jorgiño. (A) Metapelitic schists intruded by leucogranite dykes. (B) Layered garnet-bearing biotite gneiss.

**Table 1**  
Representative electron microprobe analyses (in wt%) of minerals in garnet-bearing biotite gneiss (FO1139).

Mineral	Garnet						Biotite						White mica			Chlorite			Plagioclase			Ilmenite			
	Rim	Rim	Middle	Middle	Core	Core	Core	Core	Core	Core	Core	Core	White mica	Chlorite	White mica	Chlorite	White mica	Chlorite	White mica	Chlorite	White mica	Chlorite			
SiO <sub>2</sub>	36.94	36.83	37.13	37.61	37.57	37.71	37.23	37.13	37.06	35.16	35.06	34.74	34.89	45.54	44.95	45.50	23.20	24.84	23.82	46.23	46.59	46.23	—	—	
Al <sub>2</sub> O <sub>3</sub>	21.27	21.34	21.08	21.21	21.50	21.37	21.39	21.32	21.15	18.15	18.34	18.14	18.50	24.18	34.34	33.70	21.63	20.50	20.88	33.13	32.60	32.54	—	—	
TiO <sub>2</sub>	0.03	0.00	0.05	0.02	0.05	0.07	0.03	0.05	0.07	2.63	2.44	2.42	2.48	0.21	0.26	0.00	0.09	0.14	0.06	—	—	—	52.32	52.88	
FeO	30.24	29.98	29.08	29.36	29.75	29.37	30.00	29.77	30.13	19.79	19.51	19.70	3.26	2.85	1.92	31.45	30.74	34.23	—	—	—	—	42.44	42.86	
Fe <sub>2</sub> O <sub>3</sub>	0.24	0.51	0.76	0.72	0.70	0.84	0.73	0.63	1.02	—	—	—	—	—	—	—	—	—	0.08	0.09	0.16	1.32	0.94		
MgO	2.42	2.66	2.74	3.44	3.43	3.26	2.67	2.61	2.55	10.02	10.07	9.92	10.01	0.46	0.46	0.80	10.13	12.21	8.86	—	—	—	0.09	0.06	
MnO	6.83	7.00	6.53	1.80	1.91	2.08	1.86	1.86	1.77	0.20	0.19	0.16	0.17	0.01	0.04	0.00	1.45	0.58	0.80	—	—	—	4.40	4.54	
CaO	2.68	3.11	3.91	6.57	6.70	7.04	7.41	7.44	7.50	0.00	0.01	0.00	0.03	—	—	—	—	—	—	16.89	16.83	—	—		
Na <sub>2</sub> O	0.16	0.00	0.04	0.01	0.00	0.03	0.00	0.03	0.00	0.20	0.24	0.22	0.20	0.36	0.35	0.21	—	—	—	1.91	1.94	2.06	—	—	
K <sub>2</sub> O	—	—	—	—	—	—	—	—	—	9.61	9.58	9.62	9.25	11.07	11.15	11.26	—	—	—	0.04	0.02	0.05	—	—	
BaO	—	—	—	—	—	—	—	—	0.30	0.26	0.30	0.28	0.00	0.10	0.14	—	—	—	—	—	—	—	—	—	
H <sub>2</sub> O	—	—	—	—	—	—	—	—	—	3.94	3.94	3.89	3.92	4.43	4.43	4.38	10.92	11.18	10.89	—	—	—	—	—	
Total	100.80	101.46	101.24	100.73	101.62	101.68	101.38	100.85	101.22	100.00	99.92	98.92	99.43	99.52	97.93	97.93	100.19	99.53	98.29	98.05	97.87	100.57	101.28		
Cations																									
Si	5.85	5.77	5.84	5.89	5.81	5.84	5.78	5.80	5.77	2.68	2.67	2.67	2.67	6.16	6.09	6.23	5.10	5.33	5.25	2.16	2.18	2.17	—	—	
Al																									
Ti	0.00	0.00	0.00	0.00	0.01	0.00	0.01	0.00	0.01	0.00	0.15	0.14	0.14	0.14	0.02	0.03	0.00	0.01	0.02	0.01	—	1.80	—		
Alo	3.97	3.94	3.91	3.92	3.90	3.91	3.92	3.90	3.93	3.88	0.31	0.32	0.32	0.33	0.61	3.57	3.67	2.70	2.51	2.66	—	—	—	0.99	0.99
Fe <sub>3</sub> + Fe <sub>2</sub> +	0.03	0.06	0.09	0.08	0.10	0.09	0.07	0.12	0.00	0.00	0.00	0.00	0.00	0.00	0.08	0.00	0.00	—	—	—	—	0.01	0.02	0.02	
Mg	0.57	0.64	0.64	0.80	0.79	0.75	0.62	0.61	0.59	1.14	1.14	1.14	1.14	0.09	0.09	0.16	3.32	3.91	2.91	—	—	—	0.003	0.002	
Mn	0.92	0.93	0.87	0.24	0.25	0.27	0.24	0.25	0.23	0.01	0.01	0.01	0.01	0.00	0.00	0.00	0.27	0.11	0.15	—	—	—	0.09	0.10	
Ca	0.45	0.52	0.66	1.10	1.11	1.17	1.23	1.25	1.25	0.00	0.00	0.00	0.00	0.00	0.00	0.00	—	—	—	0.85	0.84	0.85	—	—	
Na	0.05	0.00	0.01	0.00	0.00	0.01	0.01	0.01	0.01	0.00	0.03	0.04	0.03	0.03	1.91	1.93	—	—	—	0.17	0.18	0.19	—	—	
K	—	—	—	—	—	—	—	—	—	0.93	0.94	0.90	0.90	0.09	0.09	0.06	—	—	—	—	—	—	—	—	
Ba	—	—	—	—	—	—	—	—	—	0.01	0.01	0.01	0.01	0.00	0.01	0.01	—	—	—	—	—	—	—	—	
Components																									
Grossular	0.076	0.087	0.110	0.184	0.185	0.195	0.205	0.208	0.209	—	—	—	—	—	—	—	—	—	—	—	—	—	—		
Pyrope	0.095	0.104	0.107	0.134	0.132	0.126	0.103	0.101	0.099	—	—	—	—	—	—	—	—	—	—	—	—	—	—		
Almandine	0.668	0.655	0.638	0.641	0.641	0.634	0.649	0.648	0.654	—	—	—	—	—	—	—	—	—	—	—	—	—	—		
Spessartine	0.153	0.155	0.145	0.040	0.042	0.045	0.041	0.041	0.039	0.970	0.15	0.16	0.16	0.17	—	—	—	—	—	—	—	—	—		
xAl	0.993	0.985	0.977	0.979	0.980	0.976	0.979	0.981	0.970	—	—	—	—	—	—	—	—	—	—	—	—	—	—		
Muscovite	—	—	—	—	—	—	—	—	—	—	—	—	—	—	—	—	—	—	—	—	—	—	—		
wn_phlogopite	—	—	—	—	—	—	—	—	—	—	—	—	—	—	—	—	—	—	—	—	—	—	—		
Al_celadonite	—	—	—	—	—	—	—	—	—	—	—	—	—	—	—	—	—	—	—	—	—	—	—		
Fe <sub>2</sub> Al_celadonite	—	—	—	—	—	—	—	—	—	—	—	—	—	—	—	—	—	—	—	—	—	—	—		
Paragonite	—	—	—	—	—	—	—	—	—	—	—	—	—	—	—	—	—	—	—	—	—	—	—		
Ti <sub>2</sub> Mn <sub>2</sub> Ca <sub>2</sub> wm	—	—	—	—	—	—	—	—	—	—	—	—	—	—	—	—	—	—	—	—	—	—	—		
xOH	—	—	—	—	—	—	—	—	—	—	—	—	—	—	—	—	—	—	—	—	—	—	—		
xSi	—	—	—	—	—	—	—	—	—	—	—	—	—	—	—	—	—	—	—	—	—	—	—		
xMg	—	—	—	—	—	—	—	—	—	—	—	—	—	—	—	—	—	—	—	—	—	—	—		
xFe	—	—	—	—	—	—	—	—	—	—	—	—	—	—	—	—	—	—	—	—	—	—	—		
Anorthite	—	—	—	—	—	—	—	—	—	—	—	—	—	—	—	—	—	—	—	—	—	—	—		
Albite	—	—	—	—	—	—	—	—	—	—	—	—	—	—	—	—	—	—	—	—	—	—	—		
Orthoclase	—	—	—	—	—	—	—	—	—	—	—	—	—	—	—	—	—	—	—	—	—	—	—		

Structural formulae and various parameters (mainly molar fractions X of end member components) were calculated using the CALCMIN software (Brandellik, 2009) as follows: garnet, O = 24 atoms, 10 six- and eight-fold coordinated cations; biotite, O = 11, all Fe is divalent; white mica, valences = 42, cations without interlayer cations ≤ 12.1; chlorite, O = 28, all Fe is divalent; feldspar, O = 8; ilmenite, O = 3, cations = 2.

**Table 2**

Representative electron microprobe analyses (in wt%) of minerals in amphibolite (FO1140).

Mineral	Amphibole							Biotite				Plagioclase			
SiO <sub>2</sub>	48.32	47.27	48.17	47.87	48.97	45.83	49.19	48.54	34.83	34.74	35.46	36.03	46.08	45.17	46.01
Al <sub>2</sub> O <sub>3</sub>	8.33	9.59	8.52	8.97	7.66	10.77	7.62	8.10	18.39	18.44	17.46	17.04	34.07	34.96	33.94
TiO <sub>2</sub>	0.61	0.66	0.51	0.56	0.51	0.84	0.44	0.47	2.29	2.55	1.71	1.91	—	—	0.02
FeO	14.4	14.95	14.21	14.42	14.28	15.28	14.38	14.31	19.15	20.95	18.11	17.93	—	—	—
Fe <sub>2</sub> O <sub>3</sub>	—	—	—	—	—	—	—	—	—	—	—	—	0.19	0.11	0.12
MgO	13.01	12.42	13.00	13.21	13.58	11.31	13.22	12.83	9.86	9.63	13.21	13.22	—	—	—
MnO	0.16	0.23	0.26	0.17	0.22	0.18	0.29	0.24	0.11	0.19	0.12	0.06	—	—	—
CaO	11.67	11.24	11.56	11.58	11.34	11.32	11.23	11.28	—	—	—	0.04	17.38	18.38	17.51
Na <sub>2</sub> O	0.83	0.93	0.83	0.90	0.70	0.96	0.68	0.81	0.29	0.14	0.04	0.05	1.66	1.03	1.65
K <sub>2</sub> O	0.22	0.34	0.22	0.16	0.19	0.44	0.2	0.25	9.03	8.79	8.12	8.50	0.01	—	—
BaO	0.03	—	0.02	—	0.03	0.01	0.05	0.01	0.24	0.24	0.10	0.01	—	0.05	—
H <sub>2</sub> O	2.08	2.08	2.08	2.09	2.09	2.05	2.09	2.07	3.89	3.92	3.94	3.96	—	—	—
Total	99.66	99.71	99.38	99.93	99.57	98.99	99.39	98.91	98.09	99.60	98.28	98.74	99.38	99.69	99.25
Cations															
Si	6.97	6.81	6.95	6.86	7.01	6.70	7.07	7.03	2.69	2.66	2.70	2.73	2.13	2.09	2.13
Alt	1.03	1.19	1.05	1.14	0.99	1.30	0.93	0.97	1.31	1.34	1.30	1.27	1.86	1.91	1.85
Ti	0.07	0.07	0.06	0.06	0.06	0.09	0.05	0.05	0.13	0.15	0.10	0.11	—	—	—
Alo	0.38	0.43	0.40	0.37	0.31	0.55	0.36	0.42	0.36	0.32	0.26	0.25	—	—	—
Fe <sup>3+</sup>	0.64	0.83	0.69	0.82	0.85	0.67	0.79	0.67	—	—	—	0.01	—	—	—
Fe <sup>2+</sup>	1.10	0.97	1.03	0.91	0.86	1.20	0.94	1.06	1.24	1.34	1.15	1.13	—	—	—
Mg	2.80	2.67	2.80	2.82	2.90	2.46	2.83	2.77	1.13	1.10	1.50	1.49	—	—	—
Mn	0.02	0.03	0.03	0.02	0.03	0.02	0.04	0.03	0.01	0.01	0.01	—	—	—	—
Ca	1.80	1.73	1.79	1.78	1.74	1.77	1.73	1.75	—	—	—	0.86	0.91	0.87	—
Na	0.23	0.26	0.23	0.25	0.20	0.27	0.19	0.23	0.04	0.02	0.01	0.01	0.15	0.09	0.15
K	0.04	0.06	0.04	0.03	0.03	0.08	0.04	0.05	0.89	0.86	0.79	0.82	—	—	—
Ba	0.00	0.00	0.00	0.00	0.00	0.00	0.00	0.00	0.01	0.01	—	—	—	—	—
Components															
xAl	—	—	—	—	—	—	—	—	0.18	0.16	0.13	0.12	—	—	—
Anorthite	—	—	—	—	—	—	—	—	—	—	—	—	0.85	0.91	0.85
Albite	—	—	—	—	—	—	—	—	—	—	—	—	0.15	0.09	0.15
Orthoclase	—	—	—	—	—	—	—	—	—	—	—	—	0.00	0.00	0.00

Structural formulae and various parameters (mainly molar fractions X of end member components) were calculated using the CALCMIN software (Brandelik, 2009) as follows: amphibole, O = 23, cations = 13, without Ca, Na and K, stoichiometric estimation of Fe<sup>3+</sup>; for biotite, feldspar, and chlorite, see Table 1.

**Table 3**  
Bulk-rock compositions of garnet-gneiss and amphibolite.

Composition	FO1139	FO1140
(in wt%)	Garnet-gneiss	Amphibolite
SiO <sub>2</sub>	66.60	49.98
Al <sub>2</sub> O <sub>3</sub>	15.62	18.60
TiO <sub>2</sub>	0.86	1.16
Fe <sub>2</sub> O <sub>3</sub>	5.73	10.48
MnO	0.07	0.18
MgO	2.36	6.78
CaO	4.20	10.32
Na <sub>2</sub> O	1.78	0.94
K <sub>2</sub> O	1.95	0.90
P <sub>2</sub> O <sub>5</sub>	0.04	0.09
Total	99.21	99.43

frequency histogram using the Isoplot/Ex (3.41d) macro of Ludwig (2006). Monazite Th-U-Pb weighted average ages have been calculated with 95% confidence (2σ internal; see Table 4).

#### 4. Petrography and mineral chemistry

A thin-section study of the sampled metamorphic rocks confirms previous observations and lithological descriptions. In the northern segment at Morro Mejillones we recognize the occurrence of low-grade metaturbidites in the chlorite zone, and schists and gneisses with a higher-grade metamorphic overprint, in the andalusite and sillimanite zones. In the Morro Jorquín segment, from which Barrovian-type mineral zones have been described (Baeza and Pichowiak, 1988), no kyanite was identified in the samples we examined. For a detailed study we selected a garnet-biotite gneiss (sample FO1139) because it contains

fresh garnet up to several mm in diameter, and a fine-grained foliated amphibolite (sample FO1140) interleaved with gneisses.

Sample FO1139 is a fine-grained (200–700 μm) banded biotite-garnet gneiss characterized by the mineral assemblage: biotite–garnet–plagioclase–quartz–ilmenite ± white mica ± chlorite (mostly retrograde). Monazite, zircon, tourmaline, and apatite are accessory phases. Mineral inclusions in garnet are dominantly quartz, plagioclase, biotite, tourmaline, rare white mica and chlorite. Mineral associations and textures indicate that the protolith of this rock was a pelitic sediment.

Garnet (~2 vol%) occurs as clusters of up to 10 mm in mesocratic bands elongated with the predominant foliation (Fig. 3A–B). It shows irregular rims, surrounded by laths of biotite and plagioclase, and is fairly homogeneous and almandine-rich ( $X_{\text{Alm}} = 0.62\text{--}0.71$ ;  $X_{\text{Pyr}} = 0.09\text{--}0.14$ ;  $X_{\text{Gros}} = 0.09\text{--}0.21$ ;  $X_{\text{Spss}} = 0.03\text{--}0.16$ ) (Table 1). However there is a conspicuous change in the grossular and spessartine components from core to rim (Fig. 4).

Biotite occurs as fine-grained crystals with decussate texture in mica-rich layers or as isolated crystals in quartz–feldspar rich bands. On the basis of 11 oxygen atoms in the structural formula, the biotite composition is defined by the following parameters:  $\text{Al}^{\text{IV}} = 1.29\text{--}1.35$  per formula unit (pfu),  $\text{Al}^{\text{VI}} = 0.30\text{--}0.37$  pfu,  $\text{Ti}^{\text{VI}} = 0.09\text{--}0.17$  pfu; and  $X_{\text{Fe}} = \text{Fe}/(\text{Fe} + \text{Mg}) = 0.43\text{--}0.52$ . Plagioclase occurs preferentially in leuco and mesocratic bands, with a polygonal granoblastic texture displaying a homogeneous bytownite composition of  $X_{\text{An}} = 0.80\text{--}0.86$ . The polygonal texture of plagioclase suggests annealing and textural recovery of the rock after deformation. Ilmenite is relatively rich in MnO (~4.5 wt%). Retrograde chlorite replacing biotite shows variable composition with  $X_{\text{Fe}} = 0.51\text{--}0.70$ .

Rare mineral inclusions in garnet are (1) plagioclase with  $X_{\text{An}} = 0.26\text{--}0.27$ , (2) white mica with 72–82 mol% muscovite component, Si contents ranging from 3.06–3.12 pfu and Mg = 0.20–0.40 pfu,

**Table 4**  
Chemical composition of monazite grains and calculated ages resulting from electron microprobe dating of garnet-bearing biotite gneiss (FO1139).

Grain N°	#1	#2	#3	#6	#7	#8	#9	#10	#11	#12	#18
SiO <sub>2</sub>	0.42	0.41	0.42	0.51	0.52	0.49	0.53	0.50	0.52	0.53	0.46
P2O <sub>5</sub>	29.95	29.65	29.80	29.36	29.21	29.24	29.29	29.12	28.84	28.89	29.12
SO <sub>3</sub>	0.03	0.03	0.02	0.03	0.03	0.02	0.03	0.04	0.02	0.02	0.01
CaO	0.70	0.68	0.73	0.96	0.93	0.95	0.97	0.90	0.93	0.90	0.60
Y2O <sub>3</sub>	2.35	2.28	2.28	2.62	2.50	2.51	2.47	2.29	2.52	2.40	2.19
La2O <sub>3</sub>	12.29	12.19	12.47	12.38	12.47	12.85	12.63	12.92	12.47	12.46	12.41
Ce2O <sub>3</sub>	26.43	26.92	26.65	26.58	26.72	26.75	26.67	27.23	26.87	26.87	26.93
Pr2O <sub>3</sub>	3.06	3.10	3.03	2.81	2.81	2.77	2.82	2.86	2.82	2.86	3.07
Nd2O <sub>3</sub>	13.64	13.73	13.57	11.88	11.85	11.56	11.67	11.59	11.64	11.64	13.71
Sm2O <sub>3</sub>	2.90	2.88	2.86	2.38	2.30	2.22	2.27	2.24	2.27	2.26	2.76
Gd2O <sub>3</sub>	2.34	2.34	2.34	1.99	1.90	1.88	1.87	1.81	1.93	1.85	2.24
Dy2O <sub>3</sub>	0.98	0.98	0.96	1.01	0.95	0.94	0.95	0.89	0.96	0.94	0.92
PbO	0.041	0.031	0.031	0.053	0.052	0.054	0.055	0.045	0.053	0.058	0.032
ThO <sub>2</sub>	3.16	2.87	3.03	5.07	5.18	5.13	5.35	4.92	4.98	5.39	2.80
UO <sub>2</sub>	0.48	0.44	0.46	0.53	0.50	0.54	0.53	0.46	0.48	0.51	0.42
Total	98.75	98.51	98.69	98.16	97.93	97.88	98.10	97.95	97.22	97.62	97.66
Si	0.02	0.02	0.02	0.02	0.02	0.02	0.02	0.02	0.02	0.02	0.02
P	0.99	0.99	0.99	0.98	0.98	0.98	0.98	0.98	0.98	0.98	0.99
S	0.00	0.00	0.00	0.00	0.00	0.00	0.00	0.00	0.00	0.00	0.00
Σ	1.01	1.01	1.01	1.01	1.01	1.00	1.00	1.01	1.00	1.00	1.00
Ca	0.03	0.03	0.03	0.04	0.04	0.04	0.04	0.04	0.04	0.04	0.03
Y	0.05	0.05	0.05	0.06	0.06	0.05	0.05	0.05	0.05	0.05	0.05
La	0.18	0.18	0.18	0.18	0.18	0.19	0.19	0.19	0.18	0.18	0.18
Ce	0.38	0.39	0.38	0.39	0.39	0.39	0.39	0.39	0.40	0.39	0.39
Pr	0.04	0.04	0.04	0.04	0.04	0.04	0.04	0.04	0.04	0.04	0.04
Nd	0.19	0.19	0.19	0.17	0.17	0.16	0.17	0.17	0.17	0.17	0.20
Sm	0.04	0.04	0.04	0.04	0.03	0.03	0.03	0.03	0.03	0.03	0.04
Gd	0.03	0.03	0.03	0.03	0.03	0.03	0.02	0.02	0.03	0.02	0.03
Dy	0.01	0.01	0.01	0.01	0.01	0.01	0.01	0.01	0.01	0.01	0.01
Pb	0.00	0.00	0.00	0.00	0.00	0.00	0.00	0.00	0.00	0.00	0.00
Th	0.03	0.03	0.03	0.05	0.05	0.05	0.05	0.04	0.05	0.05	0.03
U	0.00	0.00	0.00	0.00	0.00	0.00	0.00	0.00	0.00	0.00	0.00
Σ	0.99	0.99	0.99	0.99	0.99	0.99	0.99	0.99	1.00	1.00	1.00
AGE	207.02	172.35	161.27	186.54	180.22	186.2	183.98	168.45	192.57	196.97	180.49
1σ	10.3	11.06	10.36	7.01	6.98	6.92	6.75	7.3	7.28	6.76	11.09
Grain N°	#19	#20	#24	#25	#26	#27	#28	#29	#30	#31	#33
SiO <sub>2</sub>	0.48	0.47	0.47	0.50	0.50	0.47	0.51	0.50	0.39	0.43	0.47
P2O <sub>5</sub>	28.76	29.23	29.15	28.87	29.00	29.16	29.57	29.53	29.58	29.51	29.41
SO <sub>3</sub>	0.03	0.02	0.03	0.03	0.03	0.02	0.04	0.02	0.03	0.02	0.03
CaO	0.68	1.00	0.82	0.96	0.96	0.93	0.98	0.93	0.76	0.77	0.96
Y2O <sub>3</sub>	2.29	2.98	2.25	2.45	2.45	2.43	2.54	2.25	2.07	2.61	2.23
La2O <sub>3</sub>	12.28	12.01	12.88	12.43	12.54	12.42	12.21	12.84	13.69	12.68	12.83
Ce2O <sub>3</sub>	26.63	25.96	27.28	26.64	26.56	26.74	26.31	27.11	28.22	26.84	26.99
Pr2O <sub>3</sub>	3.09	2.80	2.82	2.80	2.79	2.94	2.87	2.91	2.93	2.88	2.78
Nd2O <sub>3</sub>	13.57	11.57	11.82	11.77	11.70	11.86	11.75	11.60	11.54	11.32	11.36
Sm2O <sub>3</sub>	2.75	2.37	2.31	2.34	2.31	2.34	2.31	2.19	2.12	2.21	2.13
Gd2O <sub>3</sub>	2.27	2.06	1.84	1.93	1.89	1.95	1.81	1.67	1.84	1.84	1.75
Dy2O <sub>3</sub>	0.96	1.10	0.93	0.95	0.96	0.95	0.97	0.90	0.83	0.99	0.89
PbO	0.039	0.064	0.051	0.057	0.055	0.049	0.057	0.050	0.037	0.064	0.056
ThO <sub>2</sub>	3.17	5.08	4.49	4.99	5.01	4.89	5.27	4.87	3.62	4.48	4.39
UO <sub>2</sub>	0.47	0.68	0.57	0.64	0.65	0.45	0.53	0.47	0.38	0.82	0.74
Total	97.40	97.71	97.33	97.51	97.51	97.84	97.97	97.97	97.75	97.38	97.61

Table 4 (continued)

Grain N°	#19	#20	#24	#25	#26	#27	#28	#29	#30	#31	#32	#33
Si	0.02	0.02	0.02	0.02	0.02	0.02	0.02	0.02	0.02	0.02	0.02	0.02
P	0.98	0.99	0.99	0.98	0.98	0.99	0.99	0.99	0.99	1.00	0.99	0.99
S	0.00	0.00	0.00	0.00	0.00	0.00	0.00	0.00	0.00	0.00	0.00	0.00
Σ	1.00	1.01	1.00	1.00	1.00	1.01	1.01	1.01	1.01	1.01	1.01	1.01
Ca	0.03	0.04	0.04	0.04	0.04	0.04	0.04	0.04	0.04	0.03	0.04	0.04
Y	0.05	0.06	0.05	0.05	0.05	0.05	0.05	0.05	0.05	0.04	0.05	0.05
La	0.18	0.18	0.19	0.18	0.19	0.18	0.18	0.19	0.20	0.18	0.19	0.19
Ce	0.39	0.38	0.40	0.39	0.39	0.39	0.38	0.39	0.41	0.39	0.39	0.39
Pr	0.05	0.04	0.04	0.04	0.04	0.04	0.04	0.04	0.04	0.04	0.04	0.04
Nd	0.19	0.16	0.17	0.17	0.17	0.17	0.17	0.17	0.16	0.16	0.16	0.16
Sm	0.04	0.03	0.03	0.03	0.03	0.03	0.03	0.03	0.03	0.03	0.03	0.03
Gd	0.03	0.03	0.02	0.03	0.03	0.03	0.03	0.02	0.02	0.02	0.02	0.02
Dy	0.01	0.01	0.01	0.01	0.01	0.01	0.01	0.01	0.01	0.01	0.01	0.01
Pb	0.00	0.00	0.00	0.00	0.00	0.00	0.00	0.00	0.00	0.00	0.00	0.00
Th	0.03	0.05	0.04	0.05	0.05	0.04	0.05	0.05	0.04	0.04	0.04	0.05
U	0.00	0.01	0.01	0.01	0.01	0.00	0.00	0.00	0.00	0.01	0.01	0.01
Σ	1.01	0.99	1.00	1.00	1.00	1.00	1.00	0.98	0.99	0.98	0.99	0.99
AGE	198.24	209.72	189.38	193.66	184.9	183.75	193.02	185.73	183.36	213	208.57	182.34
$\sigma_{\text{tot}}$	9.88	6.64	7.42	6.74	6.66	7.42	6.82	7.34	9.46	6.72	7.33	6.43
Grain N°	#34	#35	#36	#37	#38	#39	#40	#41	#42	#43	#44	#45
SiO <sub>2</sub>	0.45	0.45	0.47	0.50	0.49	0.42	0.40	0.43	0.58	0.53	0.41	0.42
P2O <sub>5</sub>	29.47	29.47	28.79	28.75	28.77	29.48	29.65	29.01	28.52	28.65	28.53	28.51
SO <sub>3</sub>	0.03	0.03	0.03	0.03	0.03	0.02	0.03	0.02	0.02	0.03	0.02	0.04
CaO	0.82	0.87	0.78	0.97	0.97	0.86	0.84	0.66	0.89	0.75	0.82	0.77
Y2O <sub>3</sub>	2.32	2.18	2.40	2.47	2.44	2.10	2.07	2.55	2.22	2.24	2.53	2.30
La2O <sub>3</sub>	12.80	12.95	12.48	12.37	12.45	13.88	13.95	12.41	12.56	12.67	12.65	13.05
Ce2O <sub>3</sub>	27.34	27.15	26.82	26.72	26.67	27.92	28.00	26.34	26.41	27.23	27.12	27.38
Pr2O <sub>3</sub>	2.86	2.80	2.90	2.83	2.84	2.86	2.86	2.88	2.88	2.91	2.87	2.98
Nd2O <sub>3</sub>	11.64	11.50	11.86	11.64	11.62	11.28	11.30	12.96	11.66	11.99	11.79	11.76
Sm2O <sub>3</sub>	2.23	2.21	2.32	2.25	2.26	2.06	2.04	2.57	2.22	2.33	2.33	2.28
Gd2O <sub>3</sub>	1.81	1.78	1.91	1.89	1.88	1.65	1.63	2.16	1.86	1.92	1.93	1.86
Dy2O <sub>3</sub>	0.93	0.88	0.94	0.95	0.93	0.82	0.80	0.97	0.88	0.92	0.98	0.93
PbO	0.048	0.054	0.052	0.058	0.055	0.040	0.037	0.041	0.058	0.047	0.046	0.041
ThO <sub>2</sub>	4.27	4.55	4.64	5.30	5.16	3.92	3.80	3.31	5.31	4.41	4.09	3.67
UO <sub>2</sub>	0.61	0.57	0.51	0.53	0.50	0.40	0.40	0.56	0.52	0.46	0.66	0.55
Total	97.64	97.44	96.89	97.25	97.07	97.72	97.82	96.85	96.60	97.08	96.79	96.55
Si	0.02	0.02	0.02	0.02	0.02	0.02	0.02	0.02	0.02	0.02	0.02	0.02
P	0.99	0.99	0.98	0.98	0.98	0.99	0.99	0.98	0.98	0.98	0.98	0.98
S	0.00	0.00	0.00	0.00	0.00	0.00	0.00	0.00	0.00	0.00	0.00	0.00
Σ	1.01	1.01	1.00	1.00	1.00	1.01	1.01	1.01	1.00	1.00	1.00	1.00
Ca	0.04	0.04	0.03	0.04	0.04	0.04	0.04	0.04	0.03	0.04	0.04	0.03
Y	0.05	0.05	0.05	0.05	0.05	0.05	0.04	0.04	0.05	0.05	0.05	0.05
La	0.19	0.19	0.19	0.18	0.18	0.20	0.20	0.18	0.19	0.19	0.19	0.20
Ce	0.40	0.40	0.40	0.39	0.39	0.41	0.41	0.39	0.39	0.40	0.40	0.41
Pr	0.04	0.04	0.04	0.04	0.04	0.04	0.04	0.04	0.04	0.04	0.04	0.04
Nd	0.17	0.16	0.17	0.17	0.16	0.16	0.16	0.17	0.16	0.17	0.17	0.17
Sm	0.03	0.03	0.03	0.03	0.03	0.03	0.03	0.03	0.03	0.03	0.03	0.03
Gd	0.02	0.02	0.02	0.02	0.02	0.02	0.02	0.02	0.02	0.02	0.02	0.02
Dy	0.01	0.01	0.01	0.01	0.01	0.01	0.01	0.01	0.01	0.01	0.01	0.01
Pb	0.00	0.00	0.00	0.00	0.00	0.00	0.00	0.00	0.00	0.00	0.00	0.00

Table 4 (continued)

Grain N°	#34	#35	#36	#37	#38	#39	#40	#41	#42	#43	#44	#45
Th	0.04	0.04	0.04	0.05	0.05	0.04	0.03	0.03	0.05	0.04	0.04	0.03
U	0.01	0.01	0.00	0.00	0.00	0.00	0.00	0.01	0.00	0.00	0.01	0.01
$\Sigma$	0.98	1.00	1.00	1.00	1.00	0.99	0.99	1.00	1.00	1.00	1.01	1.01
AGE	184.31	200.76	195.71	196.83	193.4	182.88	174.01	190.21	198.51	190.93	177.52	177.02
$1\sigma$	7.5	7.35	7.46	6.78	6.97	8.83	9.01	9.09	6.79	7.89	7.53	8.5

and (3) chlorite characterized by variable compositions with  $X_{Fe} = 0.57\text{--}0.85$ .

Sample FO1140 is a fine-grained (50–600 µm) banded biotite amphibolite in which amphibole, biotite, plagioclase and quartz occur in apparent textural equilibrium (Fig. 3C). Apatite and ilmenite are accessory phases. Because of the fine-grained assemblage and the well-defined foliation we suggest that the protolith of this rock was either a fine-grained mafic igneous rock (ferro-basalt, see Table 3) or a mafic volcanoclastic sediment.

Amphibole occurs as inclusion-free subhedral crystals, and together with the biotite, defines the foliation. The composition of amphibole is that of a magnesiohornblende characterized by  $Si = 6.70\text{--}7.07$  pfu;  $Al^{IV} = 0.93\text{--}1.30$  pfu;  $X_{Fe} = 0.22\text{--}0.32$ ;  $Ti = 0.05\text{--}0.07$ ; and  $Na = 0.19\text{--}0.27$  pfu (Table 2). Subhedral crystals of biotite are in contact with amphibole and plagioclase. The composition of the biotite is similar to those occurring in the metapelitic gneiss:  $Al^{IV} = 1.21\text{--}1.35$  pfu,  $Al^{VI} = 0.23\text{--}0.36$  pfu;  $X_{Fe} = 0.41\text{--}0.52$ , and  $Ti^{VI} = 0.09\text{--}0.15$  pfu. Plagioclase occurs as interstitial granoblastic aggregates located between amphibole, biotite and quartz and has a relatively homogeneous bytownite-anorthite composition of  $X_{An} = 0.83\text{--}0.91$ .

## 5. Pseudosection modelling and P-T constraints

To constrain the metamorphic P-T path of the Mejillones Metamorphic Complex a P-T pseudosection was calculated for the garnet-bearing biotite-gneiss sample F01139 (Table 3). This sample was selected because it exhibits compositionally zoned garnet porphyroblasts (Fig. 4) and allows us to hypothesize that at least three metamorphic stages are recorded for the high-grade recrystallization of this metapelite.

The minimum Gibbs energy for an average bulk-rock composition was calculated for a net of P-T conditions with the computer program package PERPLE\_X (Connolly, 1990). Calculations were undertaken in the system Mn-Na-Ti-Ca-K-Fe-Mg-Al-SiO-H-O for the P-T range 3–10 kbar and 500–650 °C. We used the thermodynamic data set of Holland and Powell (1998) (updated 2002) for minerals and aqueous fluid. The following solid-solution models (see Powell and Holland, 1999; Massonne, 2010), being compatible with this data set, were selected: Gt(HP) for garnet, TiBio(HP) for biotite, Opx(HP) for orthopyroxene, Chl(HP) for chlorite, IlGkPy for ilmenite, MtUl(A) for spinel, St(HP) for staurolite, Pheng(HP) for white mica, Mica(M) for paragonite, Ctd(HP) for chloritoid, hCrd for cordierite, feldspar for feldspars, Ep(HP) for epidote, GlTrTsPg for amphibole and Omph(HP) for clinopyroxene. The selection of amphibole and clinopyroxene models, amongst a number of various models for these minerals have been discussed by Massonne (2012). The maximum value for the molar fraction of muscovite in the model Mica(M) is 0.5 (see Massonne, 2010). The same parameter has been used for the paragonite component in model Pheng(HP). Migmatites were not seen in the visited outcrops and so a thermodynamic solution model for melt was not considered.

The assumed initial composition for the studied rock had to be slightly modified (Table 3) to fit the 11-component system. The CaO content was reduced according to the bulk-rock phosphorus content, assuming that these elements are bound to apatite (which is more abundant than monazite). Oxygen contents of 0.039 wt% were selected corresponding to 10%  $Fe^{3+}$  of the total iron (see Massonne et al., 2007b). The water content was set to 4 wt%, to guarantee a free hydrous fluid phase for the P-T range of the pseudosection. The final pseudosection was redrawn by smoothing curves as demonstrated by Connolly (2005).

P-T conditions were mainly derived from the contouring of the P-T pseudosection with isopleths for various chemical and modal parameters, such as the molar fraction of pyrope and grossular component in garnet or the modal content of garnet in the corresponding rock. The

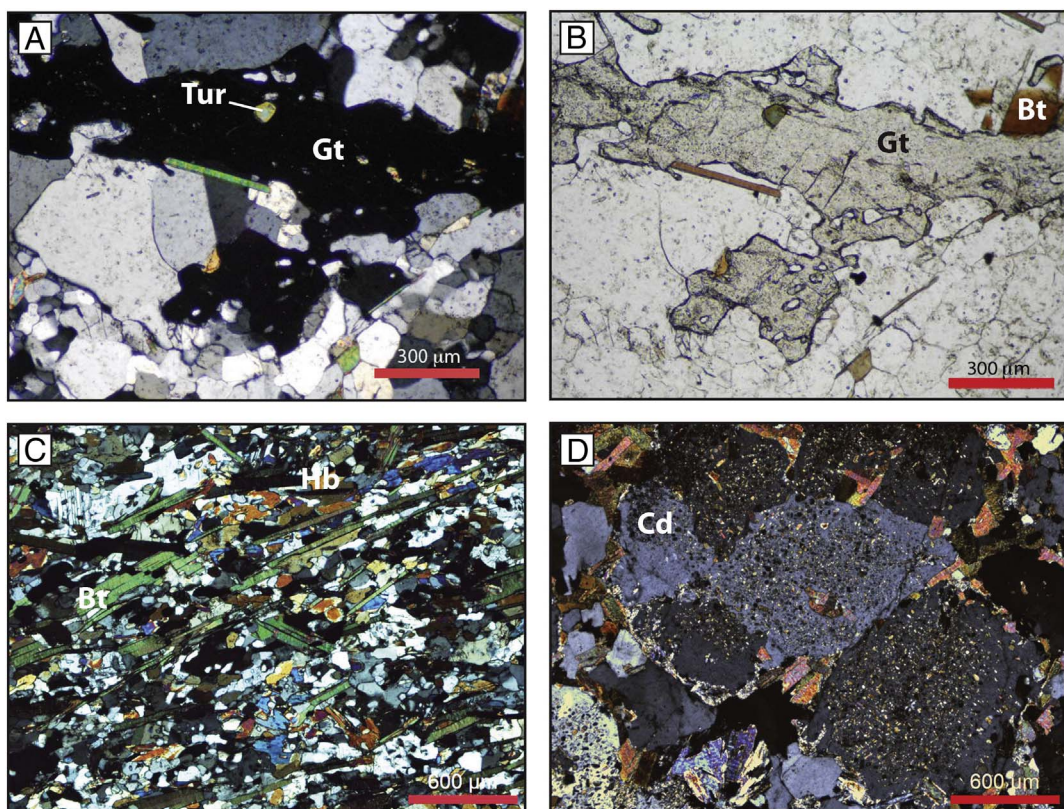


**Fig. 3.** Photomicrographs of different rocks of the Mejillones Metamorphic Complex. (A) and (B) elongated garnet porphyroblasts in quartz-plagioclase bearing band in sample FO1139. (C) Coexisting plagioclase, hornblende and biotite in amphibolites (sample FO1140). (D) Cordierite porphyroblasts with distinctive sector zoning and poikiloblastic texture (sample FO1138).

pressure error of this method, which is strongly based on the chemical analyses of garnet and mica, was estimated to be  $\pm 10\%$  of the quoted value (e.g., Massonne, 2012; Massonne et al., 2013). These errors for the quotation of an early metamorphic stage can be higher as an equilibration of the entire bulk-rock is likely for the peak metamorphic event. In addition, a temperature error of 5% of the given temperature should be considered (approximately  $\pm 30^\circ\text{C}$ ).

The prograde garnet zonation in the pelitic gneiss (Fig. 4) allows the recovery of a significant portion of the P-T history of rocks with the common mineral assemblage garnet-biotite-plagioclase-quartz-ilmenite. Fig. 5 shows the P-T pseudosection for sample FO1139 with predicted mineral assemblages. Fig. 6 displays contour lines of constant molar fractions of pyrope, almandine, spessartine and grossular, the weight percent of H<sub>2</sub>O in solids and garnet abundance in volume percent; the intersections of relevant isopleths are also indicated for geothermobarometric constraints.

The intersection of the isopleths for the molar fractions of garnet components in the core of large garnet crystals ( $X_{\text{Pyr}} = 0.102$ ;  $X_{\text{Gros}} = 0.208$ ) constrain the P-T conditions at the onset of garnet growth at 580–590 °C and 7.5–7.9 kbar. The intersection of the isopleths for the garnet middle-zone composition (core composition in smaller crystals;  $X_{\text{Pyr}} = 0.138$ ;  $X_{\text{Gros}} = 0.187$ ) indicates a prograde evolution involving a burial from 7.5–7.9 to 8.3–8.6 kbar with contemporaneous heating to 610–620 °C. The external rim composition of garnet and the intersection of corresponding isopleths ( $X_{\text{Pyr}} = 0.155$ ;  $X_{\text{Gros}} = 0.087$ ) constrain the P-T conditions during the late stage of garnet equilibration at 5.8–6.2 kbar and 630–640 °C.

## 6. Electron microprobe Th-U-Pb monazite geochronology

The electron microprobe allows a high spatial resolution which is advantageous for Th-U-Pb dating of monazite, an accessory phase

identified in the garnet-bearing gneiss sample FO1139 using the back-scattered electron detector. Monazite grains (30–80 μm) occur enclosed in plagioclase and/or in biotite, or at the contact between both phases (Fig. 7A–B).

The analyzed grains have Ce contents ranging from 0.37 to 0.41 pfu, and both La and Nd contents from 0.16–0.20 pfu. They can be classified as monazite-(Ce) (cf. Linthout, 2007). The Y<sub>2</sub>O<sub>3</sub> and ThO<sub>2</sub> contents in the analyzed grains are rather constant, varying between 2.1 and 3.0 wt %, and between 2.8 and 5.75 wt%, respectively (Table 4). Although some analyzed monazite grains are texturally homogeneous, other grains show domains with slightly different grey tones in back-scattered electron images (Fig. 7C), probably reflecting internal compositional variations.

The majority of spot ages for monazite yielded a population of Late Triassic–Early Jurassic Th-U-Pb ages, varying between 210 and 170 Ma (Fig. 8), with no systematic correspondence between the compositional variations of the grains and their calculated age. The weighted average age of 36 in-situ analyses, calculated with a confidence level of 95%, is 190 ± 4 Ma.

## 7. Discussion

The petrological investigation of garnet-bearing gneisses from the Morro Jorgiño tectonic unit resulted in an Early Jurassic Barrovian-type P-T-time trajectory during metamorphism, with peak pressure conditions of ~8–9 kbar and peak temperatures of ~610–630 °C. Our findings provide new constraints on the tectonic evolution of the northern Chilean Gondwana margin. Specifically the results confirm that rocks from Morro Jorgiño formed at significantly higher pressures than andalusite- and or sillimanite-bearing rocks at Morro Mejillones, which crystallized below 5 kbar (cf. Pattison, 1992), linked to contact metamorphism at ca. 208 Ma (Casquet et al., 2014). In this work we propose

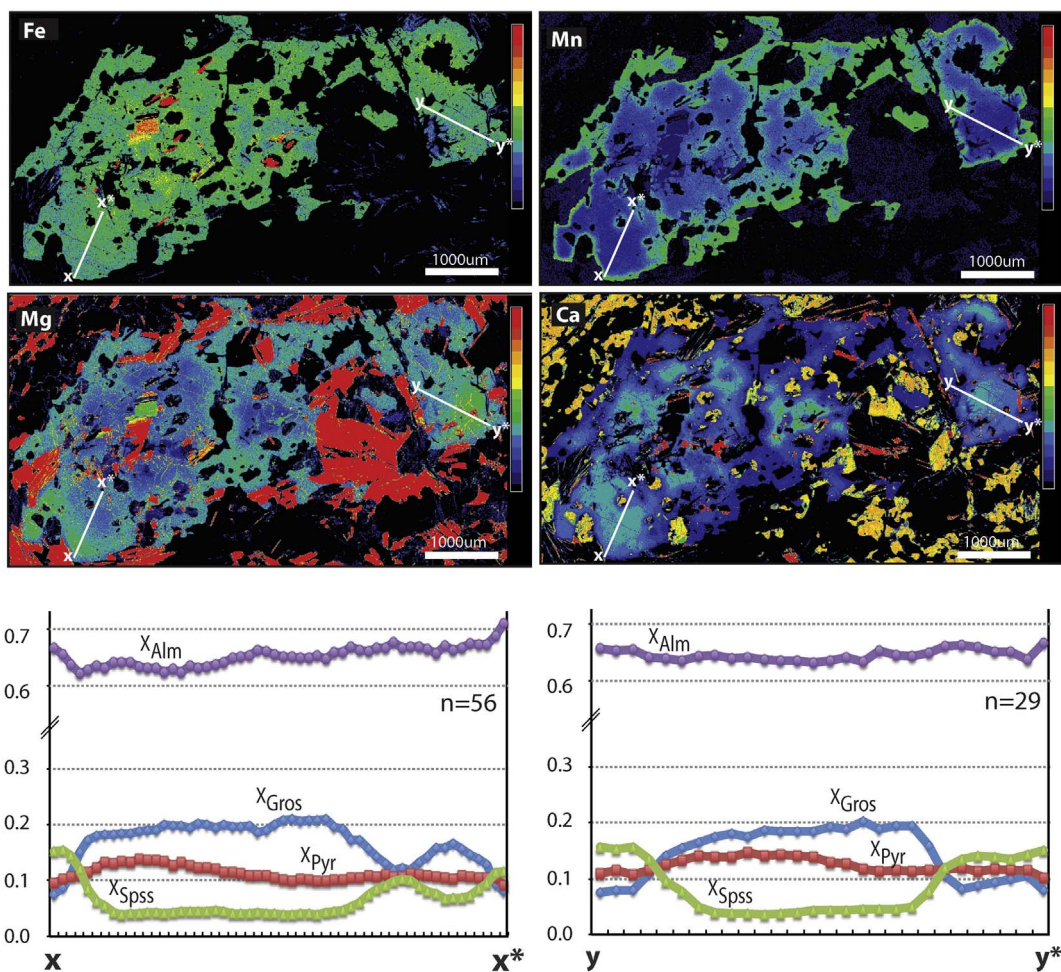


**Fig. 4.** X-ray compositional maps for Fe, Mg, Mn and Ca of garnets from pelitic gneiss sample FO1139. Red and orange colors in compositional maps represent relatively high concentration. Lowest concentrations are indicated by blue colors. Zoning profiles and their location in X-ray compositional maps of garnets are indicated. (For interpretation of the references to color in this figure legend, the reader is referred to the web version of this article.)

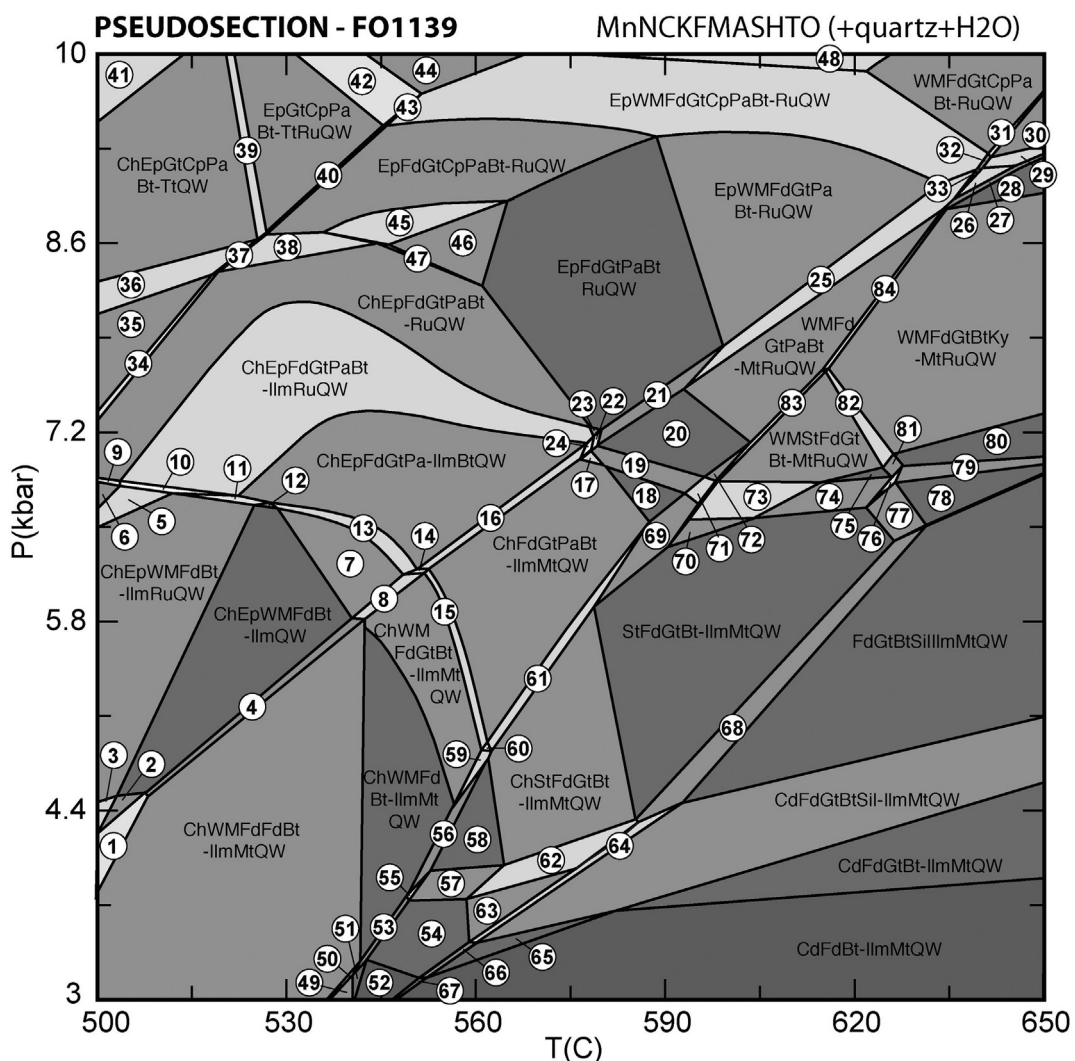
that both outcrop areas represent two genetically distinctive tectonic units formed at different times and metamorphic conditions, subsequently juxtaposed by the NW-trending Caleta Herradura fault. In the following section, we present a synthesis of the geological, petrological, and geochronological data from the Mejillones Peninsula to discuss diachronous tectonic processes and new constraints on the geodynamic evolution of the continental margin of Gondwana.

#### 7.1. P-T-time paths and metamorphic processes

We first consider rocks from the Morro Jorgiño tectonic unit. The phase diagram calculation for the garnet-biotite gneiss, with a visually estimated amount of garnet of ~2 vol%, predicts a clockwise P-T-time trajectory with a succession of three stages (M) during metamorphism: M1, 7.5–7.9 kbar and 580–590 °C; M2, 8.3–8.6 kbar and 610–620 °C; and M3, 5.8–6.2 kbar and 630–640 °C (Fig. 9).

The record of the prograde P-T-time path, after the breakdown and disappearance of chlorite, is mirrored by core and middle zone compositions of larger garnets (Fig. 4). At either M1 or M2, the internal domains of garnets should have been in equilibrium with biotite with  $X_{Fe}$  ranging between 0.37 and 0.42, thus predicting a Mg-richer composition than analyzed ( $X_{Fe}$  between 0.43 and 0.51, Fig. 8). In addition,

calculated minor phases at M1 and M2, such as epidote, white mica and rutile (Figs. 5 & 9), are not or rarely preserved in the rock. Evidently, the studied mineral assemblage, and their compositions, are related to stage M3, where diagnostic major phases like biotite with  $X_{Fe} > 0.43$  and accessory ilmenite, are predicted by the calculations. It is thus apparent that only the internal domains of the garnet (< 1 vol% of the analyzed sample) resisted the varying physiochemical conditions en route to M3. This interpretation is consistent with resorption textures, compositional zoning and decreasing mode of garnets from 5.5 vol% to 1.7 vol% (Figs. 4 & 6F), resulting from chemical dissolution and further re-precipitation at newly formed rims of garnet along the derived decompression trajectory (Fig. 9). After M3, partial chemical homogenization of biotite continued during the retrograde path at temperature of ca. 500 °C (biotite with  $X_{Fe}$  near 0.5; Fig. 9). The decompression path shown by the clockwise P-T-time evolution of Fig. 9 is preferred because the garnet-biotite gneisses are interleaved with cordierite-bearing rocks (Fig. 4C). Cordierite is a common phase in metapelites and forms at relatively low-pressure conditions (< 6 kbar; cf. Spear et al., 1999), consistent with the P-T pseudosection of sample FO1139, which predicts cordierite to occur below 5 kbar. In addition, the lack of staurolite in the rock also supports the proposed retrograde path.



## **Mineral assemblages**

- |   |                      |   |                      |   |                      |   |                     |
|---|----------------------|---|----------------------|---|----------------------|---|---------------------|
| ① | ChEpWMFdGtBt-IlmMtRu | ② | EpFdGtPaBt-IlmMtRu   | ③ | EpFdGtCpBaBt-TtRu    | ④ | StCdFdGtBtSil-IlmMt |
| ② | ChEpWMFdGtBt-Ilm     | ③ | EpFdGtPaBt-IlmRu     | ④ | EpWMGtCpPaBt-Ru      | ⑤ | CdFdBtSil-IlmMt     |
| ③ | ChEpWMFdGtBt-IlmMt   | ④ | ChEpFdGtPaBt-IlmMtRu | ⑤ | EpAmFdGtCpPaBt-Ru    | ⑥ | ChCdFdBtSil-IlmMt   |
| ④ | ChEpWMFdGtBt-IlmRu   | ⑤ | EpWMFdGtPaBt-MtRu    | ⑥ | EpAmFdGtPaBt-Ru      | ⑦ | CdFdBtAnd-IlmMt     |
| ⑤ | ChEpWMFdGtBt-IlmRu   | ⑥ | EpWMFdGtBtKy-MtRu    | ⑦ | ChEpAmFdGtPaBt-Ru    | ⑧ | StFdGtBtSil-IlmMt   |
| ⑥ | ChEpWMFdGtBt-Ru      | ⑦ | WFMFdGtBtKy-MtRu     | ⑧ | WMAmFdGtCpPaBt-Ru    | ⑨ | StFdGtPaBt-IlmMt    |
| ⑦ | ChEpWMFdGtBt-Ilm     | ⑧ | WFMFdGtBt-MtRu       | ⑨ | ChFdFdBtAnd-IlmMt    | ⑩ | WMSMFdGtBt-IlmMt    |
| ⑧ | ChEpWMFdGtBt-IlmMt   | ⑨ | WFMFdGtCpBtKy-MtRu   | ⑩ | ChWMFdFdBtAnd-IlmMt  | ⑪ | StFdGtPaBt-IlmMtRu  |
| ⑨ | ChEpWMFdGtPaBt-Ru    | ⑩ | WFMFdGtCpBtKy-Ru     | ⑪ | ChWMFdBtAnd-IlmMt    | ⑫ | StFdGtPaBt-MtRu     |
| ⑩ | ChEpWMFdGtPaBt-IlmRu | ⑪ | WFMFdGtCpPaBtKy-Ru   | ⑫ | ChFdBtAnd-IlmMt      | ⑬ | WMSMFdGtBt-IlmMtRu  |
| ⑪ | ChEpWMFdPaBt-IlmRu   | ⑫ | WFMFdGtCpPaBtKy-MtRu | ⑬ | ChWMFdBtSil-IlmMt    | ⑭ | StFdGtBt-IlmMtRu    |
| ⑫ | ChEpWMFdGtPaBt-Ilm   | ⑬ | EpWMFdGtPaBtKy-MtRu  | ⑭ | ChFdBtSil-IlmMt      | ⑮ | StFdGtBt-MtRu       |
| ⑬ | ChEpWMFdPaBt-Ilm     | ⑭ | ChEpFdGtPaBt-TtRu    | ⑮ | ChWmStFdBtSil-IlmMt  | ⑯ | StFdGtBtKy-IlmMt    |
| ⑭ | ChWMEpFdGtPaBt-IlmMt | ⑮ | ChEpFdGtPaBt-Tt      | ⑯ | ChWMSMFdBt-IlmMt     | ⑰ | StFdGtBtKy-IlmMt    |
| ⑮ | ChWMFdGtPaBt-IlmMt   | ⑯ | ChEpFdGtCpPaBt-Tt    | ⑰ | ChStFdBtSil-IlmMt    | ⑱ | FdGtBtKy-IlmMt      |
| ⑯ | ChEpFdGtPaBt-IlmMt   | ⑰ | ChEpFdGtCpPaBt-TtRu  | ⑱ | ChStFdBt-IlmMt       | ⑲ | FdGtBtKy-IlmMtRu    |
| ⑰ | ChFdGtPaBt-IlmMt     | ⑱ | ChEpFdGtCpPaBt-Ru    | ⑲ | ChWMSMFdGtBt-IlmMt   | ⑳ | FdGtBtKy-MtRu       |
| ⑱ | FdGtMicaBt-IlmMt     | ⑲ | ChEpGtCpPaBt-TtRu    | ⑳ | ChWMSMFdGtPaBt-IlmMt | ㉑ | StFdGtBtKy-MtRu     |
| ⑲ | FdGtPaBt-IlmMtRu     | ㉑ | EpGtCpPaBt-Tt        | ㉑ | ChStFdGtPaBt-IlmMt   | ㉒ | WMSMFdGtBtKy-MtRu   |
| ㉑ | FdGtPaBt-MtRu        | ㉒ | ChEpWMGtCpPaBt-Tt    | ㉒ | ChStFdGtBtSil-IlmMt  | ㉓ | WMSMFdGtPaBt-MtRu   |
| ㉒ | EpFdGtPaBt-MtRu      | ㉓ | EpWMGtCpPaBt-TtRu    | ㉓ | ChEdGtBtSil-IlmMt    | ㉔ | WMSMFdGtPaBtKy-MtRu |

**Fig. 5.** Calculated P-T pseudosection for the garnet-bearing pelitic gneiss (sample FO1139). The procedures for the P-T pseudosection calculation are indicated in the text. Mineral abbreviations are: Ab: albite; Am: amphibole; And: andalusite; Bt: biotite; Cd: cordierite; Ch: chlorite; Cp: clinopyroxene; Ep: epidote; Gt: garnet; Ilm: ilmenite; Ky: kyanite; Mt: magnetite; Fd: feldspar; Q: quartz; Ru: rutile; Sil: sillimanite; St: staurolite; Tt: titanite; Pa: paragonite; WM: white mica. The letter W is for  $H_2O$ .

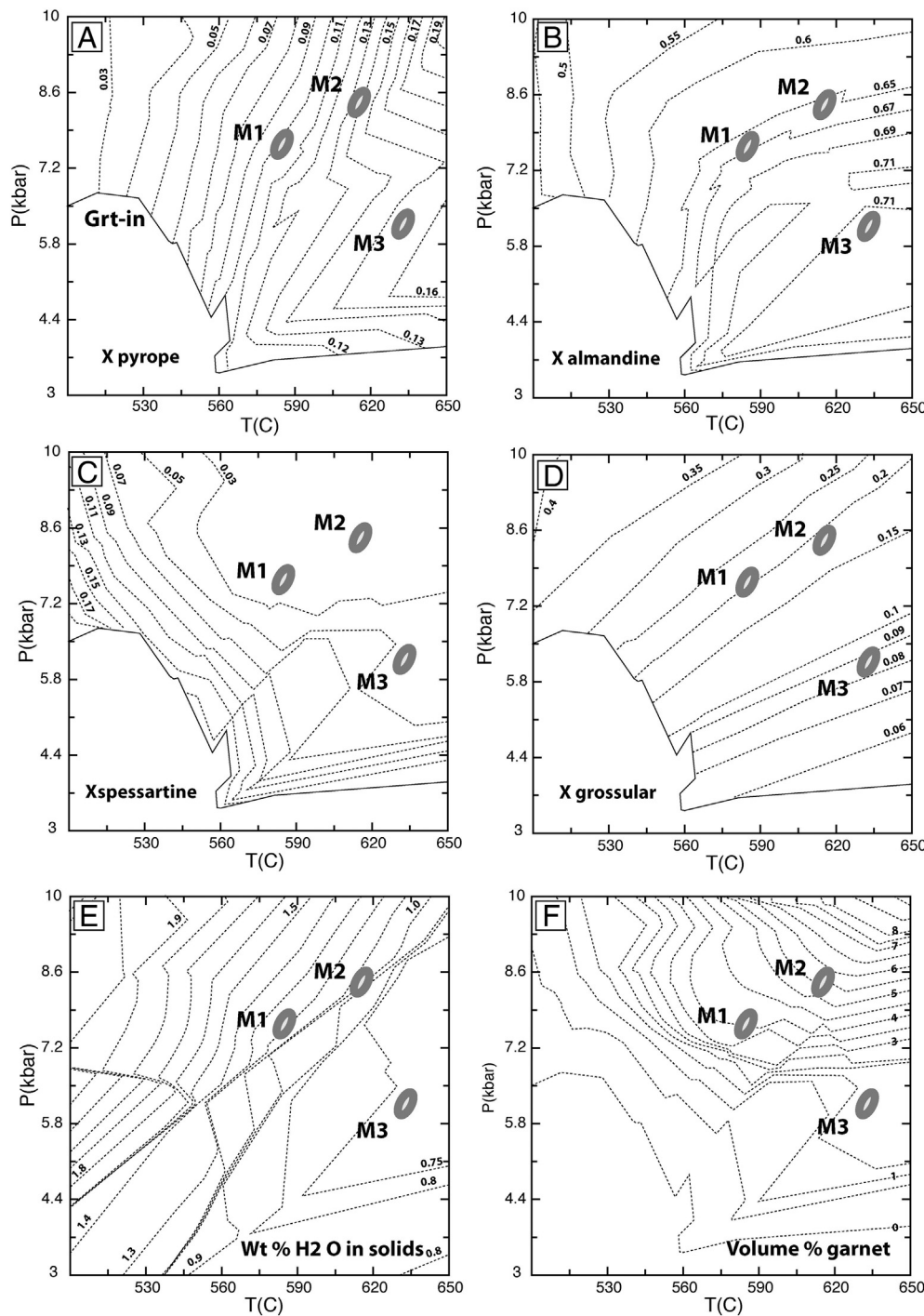


**Fig. 6.** Simplified P-T compositional space showing the contours of garnet components expressed as molar fractions of A) almandine, B) pyrope, C) spessartine and D) grossular. Also shown are contour lines for E) weight percent of H<sub>2</sub>O in solids and F) abundance of garnet in volume percent. The intersections of the isopleths for relevant contents of pyrope and grossular components analyzed with the electron microprobe, representative of the three metamorphic stages (M1, M2, M3), are also shown.

## 7.2. Age of metamorphism

Based on SHRIMP U-Pb analysis of metamorphic zircon overgrowths (with Th/U ≤ 0.06) in sample FO1139, two marked age peaks at 205–215 and 180–195 Ma are interpreted by Casquet et al. (2014) as the ages of high-grade metamorphism (Triassic) and a younger thermal isotopic perturbation during the intrusion of Lower Jurassic granitoids (Jurassic). A similarly aged thermal history is corroborated by electron microprobe monazite Th-U-Pb ages, with data ranging between 210 and 170 Ma. However, based on these closely timed zircon U-Pb ages alone, we cannot distinguish between two possible monazite generations. In contrast, our monazite analyses point to a single population, based on the relatively chemically homogeneous compositions and invariant ages

resulting in a MSWD value of 2.1 (Table 2 and Fig. 8). Moreover, this age population is characterized by Y<sub>2</sub>O<sub>3</sub> contents above 2 wt%. Massonne (2014, 2016) argued that such high Y contents point to monazite growth before garnet. In the opposite case, Y would be stored in garnet and monazite growth after garnet would no longer be saturated with Y. Thus, such monazite typically shows Y<sub>2</sub>O<sub>3</sub> contents significantly below 1 wt% (Massonne, 2014, 2016). As K-Ar dating of biotite and hornblende in metamorphic rocks from the Mejillones Metamorphic Complex point to the aforementioned influence of Jurassic intrusive events on the metamorphic rocks (Basei et al., 1996; Lucassen et al., 2000) as well, we conclude that peak and retrograde metamorphism (M2, M3) occurred just after 190 ± 4 Ma.

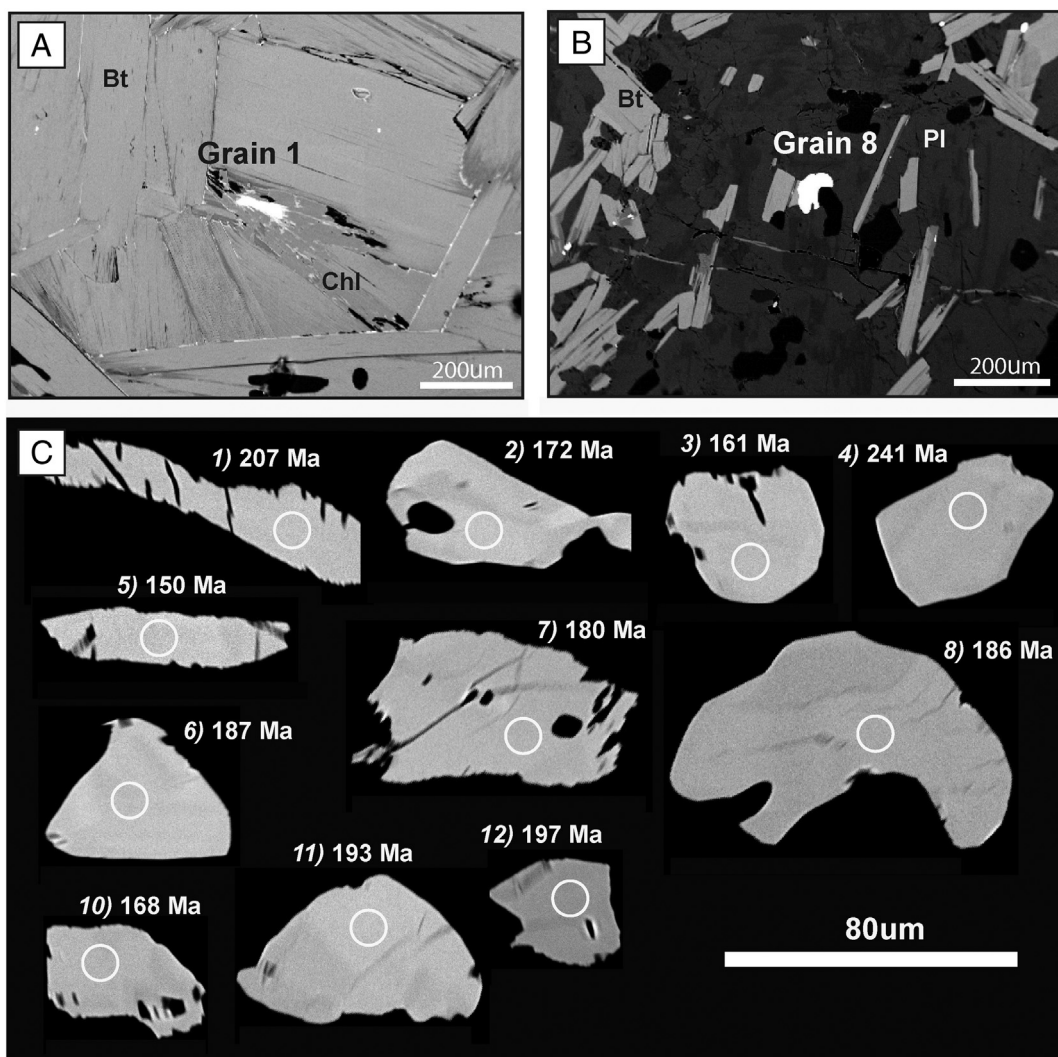


**Fig. 7.** Back-scattered electron (BSE) images showing some of the analyzed grains of monazite and their textural relation with (A) crystals of biotite (partly chloritized) and (B) plagioclase-rich domains, in the garnet-bearing gneiss (sample FO1139). The BSE of analyzed grains is shown in C).

### 7.3. Tectonic evolution

The Late Triassic to Early Jurassic metamorphism of pelitic sediments and mafic rocks of the Morro Jorgiño tectonic unit, buried to crustal depths of ~25 km, represents a previously unrecognized event.

As such, our findings elucidate the timing and metamorphic conditions on Mesozoic orogenic processes operating at the northern Chilean Gondwana margin. The disclosed P-T-time trajectory is that of a Barrovian-type metamorphism, which at its type locality (Scotland; Barrow, 1893) is associated with crustal thickening at the roots of an

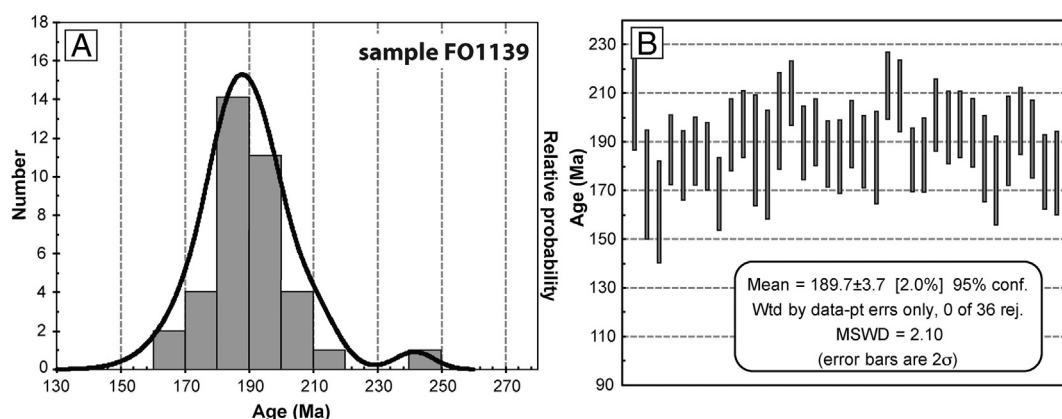


**Fig. 8.** (A) Probability density plot for all ages obtained on monazite crystals analyzed. (B) Weighted average ages, bars with  $2\sigma$  error calculated for the monazite age populations in pelitic garnet-bearing gneiss FO1139.

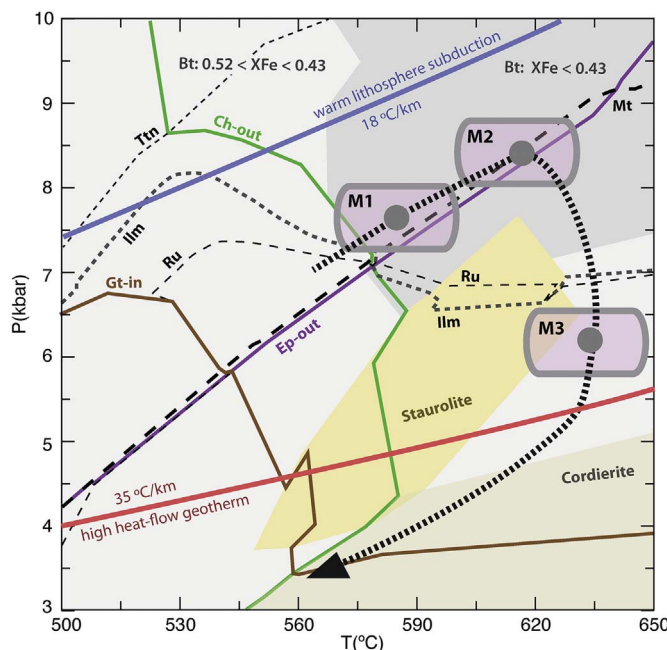


**Fig. 9.** Simplified P-T compositional for sample space showing the stability field of key mineral phases and the determined P-T-time metamorphic path of sample FO1139. Warm subduction-zone P-T trajectories and high heat-flow geotherm (Clark and Ringwood, 1964; Ernst, 2005, 2010) are indicated. Boxes in different metamorphic stages (M1, M2 and M3) indicate the assumed error for the P-T conditions estimated in this study. Abbreviations are the same than in Fig. 5.

orogenic belt during the collision and accretion of crustal fragments and island arcs along the continental margin of Laurentia (Grampian orogeny; Dewey and Ryan, 1990). Formerly, the basement rocks in the Mejillones Peninsula and those at the mouth of Río Loa (Fig. 1A) have been considered as being part of the Mejillonia terrane (Baeza, 1984), which has been interpreted as having formed elsewhere and tectonically displaced along transform faults since Late Triassic time (Ramos, 1988). Ramos (2009) postulated that the Mejillonia terrane docked against the continental margin in Paleozoic times. However, a recent geochronological study by Casquet et al. (2014) considered emplacement of Mejillonia transcurrent terrane a Mesozoic event. We propose that widespread Triassic continental extension in a retreating or stationary subduction zone (cf. Charrier et al., 2007) would have promoted the formation of thermally softened continental crust with fault-bounded crustal slivers (cf. Thompson et al., 2001). Such slivers, partially or fully detached from the continent, can subsequently interact to form small collisional and/or transpressional orogens in a supra-subduction zone (cf. Maloney et al., 2011; Calderón et al., 2012; Kato and Godoy, 2015).

The tectonic evolution of the Mejillones Metamorphic Complex is summarized in a schematic reconstruction model of the relevant continental margin (Fig. 10). The deposition of the original sedimentary successions was preceded by the final stage of the Pangea assembly and the Permian San Rafael orogeny, likely related to flat subduction dynamics (Tomlinson et al., 2012). Triassic sedimentation near the continental edge (Casquet et al., 2014) followed the post-middle Permian extensional orogenic collapse, and thus was coeval with widespread continental extension. Rifting caused the development of partitioned basins, some with episodic events of tholeiitic basaltic magmatism and development of drifted continental slivers (Mejillonia terrane) near the continental edge of a supra-subduction zone setting (Fig. 10A).

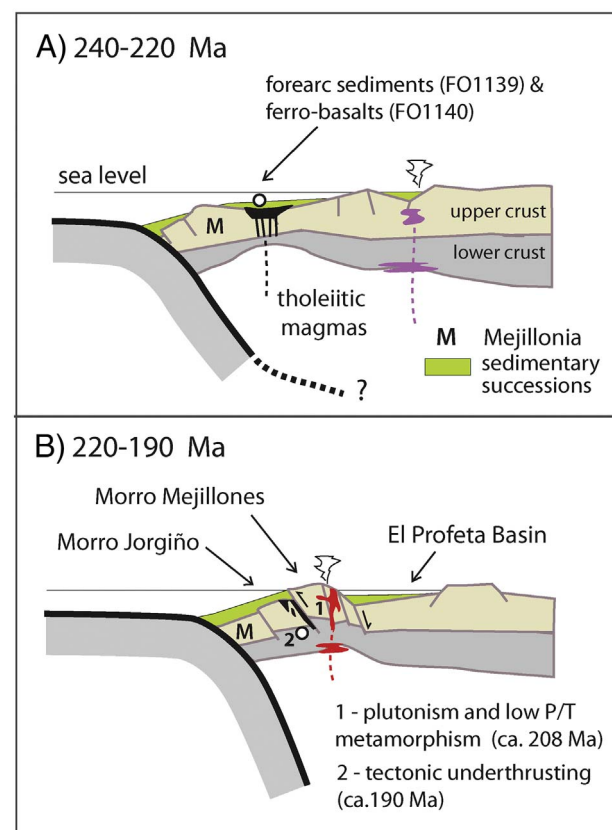


**Fig. 10.** Schematic east-west paleogeographic and tectonic reconstruction of the Gondwana margin at the latitude of Mejillones based on data and interpretations summarized in the text. (A) 240–220 Ma, generalized depositional environment of the sedimentary protoliths of the Mejillones Metamorphic Complex in a suspected marginal basin located near the continental edge; (B) 220–190 Ma, closure of the marginal basin, tectonic underthrusting of the Mejillonia terrane and crustal thickening at the continental edge of a subduction setting.

The tectonic burial of rocks from the Morro Mejillones unit occurred before the intrusion of the latest Triassic plutons (ca. 208 Ma) at shallow crustal depths (up to 12 km), as indicated by andalusite- and sillimanite-bearing contact metamorphic rocks (Fig. 10B). Plutonism was coeval with volcanism in the rift-basins and relative sea-level rise. At the same time, the burial of metasedimentary rocks of the Morro Jorgiño tectonic unit started linked probably to the tectonic underthrusting of the Mejillonia terrane (Fig. 10B). This burial reached lower crustal depths (~25 km), following a relatively “warm” geotherm of ~25 °C/km (Fig. 9) as would be expected in the forearc-arc transition of a convergent margin and/or during subduction of a still warm oceanic slab (cf. Peacock, 1996) (Fig. 10B). This process was finalized before ca. 190 Ma. The Barrovian-type decompression path for the Morro Jorgiño tectonic unit encompassed a minimum exhumation of ~10–15 km linked to rapid extensional unroofing of deeply buried crustal rocks (Fig. 9). The extensional event was probably related to transtensional deformation (Hervé, 1987; Scheuber et al., 1994) coeval with the underplating of mantle-derived mafic magmas of the Punta Tetas Complex. Mafic magmatism was accompanied by high-grade metamorphism (magmatic arc metamorphism of Lucassen and Franz, 1996) and crustal partial melting as signalized by anatexitic leucogranite dikes intruding the Morro Jorgiño unit at ca. 180 Ma.

## 8. Conclusions

Based on detailed petrography, P-T pseudosection modelling of garnet-bearing gneisses and Th-U-Pb in situ dating of monazite, we identify new evidence for Late Triassic and Early Jurassic orogenic processes acting along the convergent margin of Gondwana in northern Chile. The Morro Mejillones and Morro Jorgiño tectonic units of the Mejillones Metamorphic Complex show distinct metamorphic ages and thermal evolution. The Morro Mejillones tectonic unit was metamorphosed at low pressure conditions (andalusite-sillimanite series) during the intrusion of tonalitic plutons at ca. 208 Ma (cf. Casquet et al., 2014). Separately, the Morro Jorgiño tectonic unit underwent a Barrovian-type P-T-time history characterized by burial under epidote-amphibolite facies conditions (up to ~8–9 kbar and ~600–630 °C). Prograde metamorphism in the Morro Jorgiño block followed an elevated geotherm during crustal thickening near the continental edge of a supra-subduction zone setting, linked probably to the docking of the Mejillonia terrane. After ca. 190 Ma, metamorphic rocks of the Morro Jorgiño block experienced a late thermal overprint and rapid decompression path reaching amphibolite facies conditions (~6.0 kbar and 635 °C), coeval with the emplacement of Early Jurassic (ca. 184 Ma) plutons, in response to the extensional tectonic regime in a nascent arc environment. These processes preceded the Jurassic tectonic juxtaposition of both tectonic units through the Caleta Herradura fault, a NW-trending branch of the Atacama Fault System.

## Acknowledgements

This research is part of the FONDECYT projects 1130227 and 1095099 and the BMBF–CONICYT collaboration project CHL09/021. The constructive comments of reviewers Dr. Victor Ramos and Dr. Gerhard Franz are greatly acknowledged.

## References

- Baeza, L., 1984. Petrography and Tectonics of the Plutonic and Metamorphic Complexes of Limón Verde and Mejillones Peninsula, Northern Chile. Thesis. Universität Tübingen, Germany.
- Baeza, L., Pichowiak, S., 1988. Ancient crystalline basement provinces in the North Chilean Central Andes. Relics of continental crust development since the Mid Proterozoic. In: Bahlburg, H., Breitkreuz, C., Giese, P. (Eds.), The Southern Central Andes: Contributions to Structure and Evolution of an Active Continental Margin. Lecture Notes in Earth Sciences 17. Springer, Heidelberg, pp. 3–24.
- Barrow, G., 1893. On an intrusion of muscovite-biotite gneiss in the south-eastern highland of Scotland, and its accompanying metamorphism. Q. J. Geol. Soc. Lond. 49, 330–354.
- Basel, M.A.S., Charrier, R., Hervé, F., 1996. New ages (U-Pb, Rb-Sr, K-Ar) from supposed pre-Cambrian units in northern Chile: some geotectonic implications. In: Third International Symposium on Andean Geodynamics, Saint Malo, France, Extended Abstracts, pp. 763–766.
- Brandelik, A., 2009. CALCMIN — an EXCEL™ visual basic application for calculating mineral structural formulae from electron microprobe analyses source. Comput. Geosci. 35, 1540–1551.
- Brown, M., Díaz, F., Grocott, J., 1993. Displacement history and tectonic significance of the El Salado segment of the Atacama Fault System, Northern Chile. Geol. Soc. Am. Bull. 105, 1165–1174.
- Calderón, M., Fosdick, J., Warren, C., Fanning, C.M., Massonne, H.-J., Fadel, Cury L., Schwanethal, J., Fonseca, P., Galaz, G., Gaytán, D., Hervé, F., 2012. The low-grade Canal de las Montañas Shear Zone and its role on the tectonic emplacement of the Sarmiento Ophiolitic Complex and Late Cretaceous Patagonian Andes orogeny, Chile. Tectonophysics 524–525, 165–185.
- Casquet, C., Hervé, F., Pankhurst, R.J., Baldo, M., Calderón, M., Fanning, C.M., Rapela, C.W., Dahlquist, J., 2014. The Mejillonia suspect terrane (Northern Chile): Late Triassic fast burial and metamorphism of sediments in a magmatic arc environment extending into the Early Jurassic. Gondwana Res. 25, 1272–1286.
- Charrier, R., 1979. El Triásico en Chile y regiones adyacentes de Argentina: Una reconstrucción paleogeográfica y paleoclimática. 26. Departamento de Geología, Universidad de Chile, Comunicaciones, pp. 1–47.
- Charrier, R., Pinto, L., Rodriguez, M.P., 2007. Tectonostratigraphic evolution of the Andean Orogen in Chile. In: Moreno, T., Gibbons, W. (Eds.), The Geology of Chile, The Geological Society, London, 2007, Special Publication 4, pp. 21–114.
- Chong, G., von Hillebrandt, A., 1985. El Triásico preandino de Chile entre los 23°30' y 26°00' de lat. Sur. Actas 4º Congreso Geológico Chileno, Antofagasta. 1. pp. 1/138–1/154.
- Clark, S.P., Ringwood, A.E., 1964. Density distribution and constitution of the mantle. Rev. Geophys. 2, 35–88.
- Clift, P.D., Hartley, A.J., 2007. Slow rates of subduction erosion and coastal underplating along the Andean margin of Chile and Peru. Geology 35 (6), 503–506.
- Connolly, J.A.D., 1990. Multivariable phase diagrams; an algorithm based on generalized thermodynamics. Am. J. Sci. 290, 666–718.
- Connolly, J.A.D., 2005. Computation of phase equilibria by linear programming: a tool for geodynamic modeling and its application to subduction zone decarbonation. Earth Planet. Sci. Lett. 236, 524–541.
- Contreras, J.P., Espinoza, M., De la Cruz, R., Jorquera, R., Kraus, S., Ramírez, C., Naranjo, J.A., Escribano, J., Martínez, P., 2013. Carta Cifuncho, Regiones de Antofagasta y Atacama. Carta Geológica 1:100.000, SERNAGEOMIN, Santiago.
- Cortés, J.C., Marquardt, C.R., González, G.L., Wilke, H.-G.H., Marinovic, N., 2007. Carta Mejillones y Península Mejillones. Región de Antofagasta. Carta Geológica de Chile 1:100.000, SERNAGEOMIN, Santiago.
- Damm, W., Pichowiak, S., Harmon, R.S., Todt, W., Kelley, S., Omarini, R., Niemeyer, H., 1990. Pre-Mesozoic evolution of the Central Andes, the basement revisited. In: Mahlburg, K.S., Rapela, C.W. (Eds.), Plutonism From Antarctica to Alaska. Geological Society of America, Special Papers 241. pp. 101–126.
- Del Rey, A., Deckart, K., Arriagada, C., Martínez, F., 2016. Resolving the paradigm of the late Paleozoic–Triassic Chilean magmatism: isotopic approach. Gondwana Res. 37, 172–181.
- Dewey, J.F., Ryan, P.D., 1990. The Ordovician evolution of the South Mayo Trough, western Ireland. Tectonics 9, 887–901.
- Ernst, W.G., 2005. Alpine and Pacific styles of Phanerozoic mountain building: subduction-zone petrogenesis of continental crust. Terra Nova 17, 165–188.
- Ernst, G., 2010. Subduction-zone metamorphism, calc-alkaline magmatism, and convergent-margin crustal evolution. Gondwana Res. 25 (1), 8–16.
- Escribano, J., Martínez, P., Domagala, J., Padel, M., Espinoza, M., Jorquera, R., Contreras, J., De la Cruz, R., Calderón, M., 2013. Cartas Bahía Isla Blanca y Taltal, Región de Antofagasta. Carta Geológica 1:100.000, SERNAGEOMIN, Santiago.
- Firth, E., Holwell, D.A., Oliver, N.H.S., Mortensen, J.K., Rovardi, M.P., Boyce, A.J., 2015. Constraints on the development of orogenic style gold mineralisation at Mineral de Talca, Coastal Range, central Chile: evidence from a combined structural, mineralogical, S and Pb isotope and geochronological study. Mineral. Deposita 50, 675–696.
- Gana, P., 1991. Magmatismo bimodal del Triásico Superior — Jurásico Inferior. Rev. Geol. Chile 18, 55–67.
- García, F., 1967. Geología del Norte Grande de Chile. In: Simposio sobre el Geosinclinal Andino 1962. Sociedad Geológica de Chile Publicación 3 (Santiago).
- Godoy, E., Lara, L., 1998. Hojas Chanáral y Diego de Almagro, Región de Atacama. Servicio Nacional de Geología y Minería, Santiago, Chile. 1:100.000. pp. 5–6.
- Gregori, D., Benedini, L., 2013. The Cordon del Portillo Permian magmatism, Mendoza, Argentina, plutonic and volcanic sequences at the western margin of Gondwana. J. S. Am. Earth Sci. 42, 61–73.
- Hartley, A.J., Jolley, E.J., 1995. Tectonic implications of late Cenozoic sedimentation from the Coastal Cordillera of northern Chile (22°–24°S). J. Geol. Soc. Lond. 152, 51–63.
- Hervé, M., 1987. Movimiento sinistral en el Cretácico Inferior de la Zona de Falla de Atacama al norte de Paposo (24°S), Chile. Rev. Geol. Chile 31, 37–42.
- Hervé, F., Faúndez, V., Calderón, M., Massonne, H.-J., Willner, A., 2007. Metamorphic and plutonic basement complexes. In: Moreno, T., Gibbons, W. (Eds.), The Geology of Chile Geological Society, London, pp. 5–20.
- Hervé, F., Fanning, C.M., Calderón, M., Mpodozis, C., 2014. Early Permian to Late Triassic batholiths of the Chilean Frontal Cordillera (28°–31°S): SHRIMP U-Pb zircon ages and Lu-Hf and O isotope systematics. Lithos 184–187, 436–446.
- Holland, T.J.B., Powell, R., 1998. An internally consistent thermodynamic data set for phases of petrological interest. J. Metamorph. Geol. 16, 309–343.
- Kato, T., Godoy, E., 2015. Middle to late Triassic mélangé exhumation along a pre-Andean transpressional fault system: coastal Chile (26°–42° S). Int. Geol. Rev. 57, 606–628.
- Li, Z.X., Powell, C.M., 2001. An outline of the palaeogeographic evolution of the Australasian region since the beginning of the Neoproterozoic. Earth-Sci. Rev. 53, 237–277.
- Linthout, K., 2007. Tripartite division of the system  $\text{REEPO}_4\text{-CaTh}(\text{PO}_4)_2\text{-2ThSiO}_4$ , discreditation of brabantite, and recognition of cheralite as the name of members dominated by  $\text{CaTh}(\text{PO}_4)_2$ . Can. Mineral. 45, 503–508.
- Llambías, E.J., Sato, A.M., 1995. El batolito de Colanguil: transición entre orogénesis y anorogénesis. Rev. Asoc. Geol. Argent. 50, 111–131.
- Lucassen, F., Franz, G., 1996. Magmatic arc metamorphism: petrology and temperature history of metabasic rocks in the Coastal Cordillera of northern Chile. J. Metamorph. Geol. 14, 249–265.
- Lucassen, F., Franz, G., Laber, A., 1999. Permian high pressure rocks — the basement of the Sierra de Limón Verde in Northern Chile. J. S. Am. Earth Sci. 12, 183–199.
- Lucassen, F., Beccio, R., Wilke, H.G., Franz, G., Thirlwall, M.F., Viramonte, J., Wemmer, K., 2000. Proterozoic–Paleozoic development of the basement of the Central Andes (18°–26°S) — a mobile belt of the South American craton. J. S. Am. Earth Sci. 13, 697–715.
- Lucassen, F., Beccio, R., Franz, G., 2011. The Early Palaeozoic high-grade metamorphism at the active continental margin of West Gondwana in the Andes (NW Argentina/N Chile). Int. J. Earth Sci. (Geol. Rundsch) 100, 445–463.
- Ludwig, K.R., 2006. Isoplot/Ex Version 3.41d: A Geochronological Toolkit for Microsoft Excel, Berkeley Geochronology Center. Special Publication. 4.
- Maksaev, V., Munizaga, F., Tassinari, C., 2014. Timing of the magmatism of the paleo-Pacific border of Gondwana: U-Pb geochronology of Late Paleozoic to Early Mesozoic igneous rocks of the north Chilean Andes between 20° and 31°S. Andean Geol. 41, 447–506.
- Maloney, K.T., Clarke, G.L., Klepeis, K.A., Fanning, C.M., Wang, W., 2011. Crustal growth during back-arc closure: cretaceous exhumation history of Cordillera Darwin, southern Patagonia. J. Metamorph. Geol. 29 (6), 649–672.
- Marinovic N., Smoje I., Maksaev V., Hervé M. and Mpodozis C., Hoja Aguas Blancas, Región de Antofagasta. Carta Geológica de Chile 70 1:250.000, SERNAGEOMIN, Santiago, 1995.
- Massonne, H.-J., 2010. Phase relations and dehydration behaviour of calcareous

- sediments at very-low to low grade metamorphic conditions. *Periodico di Mineralogia* 79 (2), 21–43.
- Massonne, H.-J., 2012. Formation of amphibole and clinozoisite–epidote in eclogite owing to fluid infiltration during exhumation in a subduction channel. *J. Petrol.* 53, 2115–2138.
- Massonne, H.-J., 2014. Wealth of P-T-t information in medium-high grade metapelites: example from the Jubrique Unit of the Betic Cordillera, S Spain. *Lithos* 208–209, 137–157.
- Massonne, H.-J., 2016. Tertiary high-pressure metamorphism recorded in andalusite-bearing micaschist, southern Pirin Mts., SW Bulgaria. *Eur. J. Mineral.* (in press).
- Massonne, H.-J., Kennedy, A., Nasdala, L., Theye, T., 2007a. Dating of zircon and monazite from diamondiferous quartzfeldspathic rocks of the Saxonian Erzgebirge. *Mineral. Mag.* 71, 407–425.
- Massonne, H.-J., Willner, A., Gerya, T., 2007b. Densities of metapelitic rocks at high to ultrahigh pressure conditions: what are the geodynamic consequences? *Earth Planet. Sci. Lett.* 256, 12–27.
- Massonne, H.-J., Opitz, J., Theye, T., Nasir, S., 2013. Evolution of a very deeply subducted metasediment from As Sifah, northeastern coast of Oman. *Lithos* 156–159, 171–185.
- Morandé, J.P., 2014. El Basamento pre-Mesozoico de la Sierra Limón Verde: Implicancias Para la Evolución Tectónica del Norte de Chile. Tesis Para Optar al Grado de Magíster en Ciencias. Mención Geología. Universidad de Chile, Santiago (99 pp.).
- Mpodozis, C., Ramos, V.A., 1989. The Andes of Chile and Argentina. In: Erickson, G.E., Cañas, M.T., Reinemund, J.A. (Eds.), Geology of the Andes and its relation to hydrocarbon and energy resources. Earth Science Series Vol. 11. Circum-Pacific Council for Energy and Hydrothermal Resources, American Association of Petroleum Geologists, Houston, Texas, pp. 59–90.
- Munizaga, F., Maksaev, V., Fanning, C.M., Giglio, S., Yaxley, G., Tassinari, C.C.G., 2008. *Gondwana Res.* 13, 407–427.
- Murphy, J.B., Nance, R.M., Cawood, P.A., 2009. Contrasting modes of supercontinent formation and the conundrum of Pangea. *Gondwana Res.* 15, 408–420.
- Naranjo, J., Puig, A., 1984. Hoja Tal Tal y Chanalar. Servicio Nacional de Geología y Minería, Santiago, Carta Geológica de Chile. pp. 62–63 (140 p.).
- Oliveros, V., Morata, D., Aguirre, L., Féraud, G., Fornanri, M., 2007. Jurassic to Early Cretaceous subduction-related magmatism in the Coastal Cordillera of northern Chile (18°30'–24°S): geochemistry and petrogenesis. *Rev. Geol. Chile* 34 (2), 209–232.
- Pankhurst, R.J., Hervé, F., Fanning, C.M., Calderón, M., Niemeyer, H., Griem-Klee, S., Soto, F., 2016. The pre-Mesozoic rocks of northern Chile: U-Pb ages, and Hf and O isotopes. *Earth Sci. Rev.* 152, 88–105.
- Parada, M.A., López-Escobar, L., Oliveros, V., Fuentes, F., Morata, D., Calderón, M., Aguirre, L., Féraud, G., Espinoza, F., Moreno, H., Figueroa, O., Muñoz Ravo, J., Troncoso Vásquez, R., Stern, C.R., 2007. Andean Magmatism. In: Moreno, T., Gibson, W. (Eds.), The Geology of Chile. Special Publication 4. The Geological Society, London, pp. 115–146.
- Pattison, D.R.M., 1992. Stability of andalusite and sillimanite and the Al<sub>2</sub>SiO<sub>5</sub> triple point: constraints from the Ballachulish aureole, Scotland. *J. Geol.* 100, 423–446.
- Peacock, S.M., 1996. Thermal and petrologic structure of subduction zones. In: Bebout, G.E., Scholl, D.W., Kirby, S.H., Platt, J.P. (Eds.), Subduction Top to Bottom. Geophysical Monograph 96 American Geophysical Union.
- Powell, R., Holland, T., 1999. Relating formulations of the thermodynamics of mineral solid solutions: activity modeling of pyroxenes, amphiboles and micas. *Am. Mineral.* 84, 1–14.
- Ramos, V.A., 1988. Late Proterozoic – Early Paleozoic of South America – a collisional history. *Episodes* 11, 168–174.
- Ramos, V.A., 2009. Anatomy and global context of the Andes: main geologic features and the Andean orogenic cycle. *Geol. Soc. Am. Mem.* 204, 31–65.
- Scheuber, E., González, G., 1999. Tectonics of the Jurassic—Early Cretaceous magmatic arc of the north Chilean Coastal Cordillera (22°–26° S): a story of crustal deformation along a convergent plate boundary. *Tectonics* 18, 895–910.
- Scheuber, E., Bogdanic, T., Jensen, A., Reutter, K.J., 1994. Tectonic development of the North Chilean Andes in relation to plate convergence and magmatism since the Jurassic. In: Reutter, K.-J., Scheuber, E., Wigger, P. (Eds.), Tectonics of the Southern Central Andes. Structure and Evolution of an Active Continental Margin Springer, Heidelberg, pp. 121–140.
- SERNAGEOMIN, 2003. Mapa Geológico de Chile: versión digital. publicación geológica digital, No. 4, 2003. CDROM, versión 1.0, 2003. Base Geológica escala 1:1.000.000. Gobierno de Chile, Servicio Nacional de Geología y Minería, Subdirección Nacional de Geología.
- Soto, M.F., 2013. Pressure–Temperature–Time Paths of the Limón Verde Metamorphic Complex, Chile (Tesis) de Grado de Magíster en Ciencias, Mención Geología, Departamento de Geología, Universidad de Chile, Santiago (125 pp.).
- Spear, F.S., Kohn, M.J., Cheney, J.T., 1999. P-T paths from anatetic pelites. *Contrib. Mineral. Petro.* 134, 17–32.
- Suárez, M., Bell, M., 1992. Triassic rift-related sedimentary basins in northern Chile (24°–29°S). *J. S. Am. Earth Sci.* 6, 109–121.
- Thompson, A.B., Schulmann, K., Jezek, J., Tolar, V., 2001. Thermally softened continental extension zones (arc and rifts) as precursors to thickened orogenic belts. *Tectonophysics* 332, 115–141.
- Tomlinson, A.J., Blanco, N., 2008. Geología de la Franja El Abra–Chuquicamata, II Región (21° 45' – 22° 30' S). Servicio Nacional de Geología y Minería, Informe Registrado IR-08-35, Santiago. (196 pp.).
- Tomlinson, A.J., Blanco, N., García, M., Baeza, L., Alcota, H., Ladino, M., Pérez de Arce, C., Fanning, C.M., Martin, M.W., 2012. Permian exhumation of metamorphic complexes in the Calama area: evidence for flat-slab subduction in northern Chile during the San Rafael tectonic phase and origin of the Central Andean Gravity High. In: XIII Congreso Geológico Chileno, Antofagasta, Electronic Expanded Abstracts, thematic Session. T2, pp. 209–211.
- Uliana, M.A., Biddle, K.T., 1988. Mesozoic–Cenozoic paleogeographic and geodynamic evolution of southern south America. *Rev. Bras. Geosci.* 18 (2), 172–190.
- Vásquez, P., Gladny, J., Franz, G., Frei, D., Romer, R.L., 2011. Early Mesozoic Plutonism of the Cordillera de la Costa (34°–37°S), Chile: constraints on the onset of the Andean Orogeny. *J. Geol.* 119 (2), 159–184.
- Vergara, M., López-Escobar, L., Cancino, A., Levi, B., 1991. The Pichidangui Formation; some geochemical characteristics and tectonic implications of the Triassic marine volcanism in central Chile (31°55' to 32°20'S). In: Harmon, R.S., Rapela, C.W. (Eds.), Andean Magmatism and Its Tectonic Setting. Geological Society of America, Special Paper Vol. 265, pp. 93–98.
- Vicente, J.C., 2006. Dynamic paleogeography of the Jurassic Andean basin: pattern of regression and general considerations on main features. *Rev. Asoc. Geol. Argent.* 61 (3), 408–437.
- Villegas, J., Parada, M.A., 1993. La superunidad Limarí: aspectos litológicos y de emplazamiento del plutonismo Triásico Superior–Jurásico Inferior de Chile Central. *Comunicaciones* 44, 29–48.
- Willner, A., Massonne, H.-J., Ring, U., Sudo, M., Thomson, S.N., 2011. P-T evolution and timing of a late Paleozoic fore-arc system and its heterogenous Mesozoic overprint in north-central Chile (latitudes 31°–32°S). *Geol. Mag.* 149, 177–207.
- Winkler, H.G.F., 1976. Petrogenesis of Metamorphic Rocks. Springer-Verlag (334 pp.).